ARTICLE

doi:10.1038/nature17975

Crystal structure of the epithelial calcium channel TRPV6

Kei Saotome[1]*, Appu K. Singh[1]*, Maria V. Yelshanskaya[1] & Alexander I. Sobolevsky[1]

Precise regulation of calcium homeostasis is essential for many physiological functions. The Ca^{2+}-selective transient receptor potential (TRP) channels TRPV5 and TRPV6 play vital roles in calcium homeostasis as Ca^{2+} uptake channels in epithelial tissues. Detailed structural bases for their assembly and Ca^{2+} permeation remain obscure. Here we report the crystal structure of rat TRPV6 at 3.25 Å resolution. The overall architecture of TRPV6 reveals shared and unique features compared with other TRP channels. Intracellular domains engage in extensive interactions to form an intracellular 'skirt' involved in allosteric modulation. In the K^+ channel–like transmembrane domain, Ca^{2+} selectivity is determined by direct coordination of Ca^{2+} by a ring of aspartate side chains in the selectivity filter. On the basis of crystallographically identified cation–binding sites at the pore axis and extracellular vestibule, we propose a Ca^{2+} permeation mechanism. Our results provide a structural foundation for understanding the regulation of epithelial Ca^{2+} uptake and its role in pathophysiology.

The TRP channels are a superfamily of cation-permeable ion channels that are widely known for their role as transducers of sensory modalities[1]. TRPV5 and TRPV6 are TRP channels that are uniquely selective for Ca^{2+} (permeability ratio $P_{Ca}/P_{Na} > 100$) (ref. 2). They have not been reported to be responsive to temperature, tastants or odours, but the mechanosensitive properties of TRPV6 appear to be important for the formation of microvilli[3]. TRPV5 and TRPV6 belong to the vanilloid subfamily of TRP channels, share ~75% sequence identity and are involved in the transport of calcium through epithelial cell membranes[4]. Knockout of TRPV6 in mice leads to various phenotypes linked to impaired Ca^{2+} homeostasis, including defective intestinal Ca^{2+} absorption, lower body weight, impaired fertility and dermatitis[5–8]. Altered TRPV6 expression has also been shown in various transgenic mouse models of human diseases[8], including Crohn's and kidney stone diseases. In addition, TRPV6 is implicated in the development and progression of numerous forms of cancer, and its overexpression pattern correlates with the aggressiveness of the disease[9,10]. Accordingly, TRPV6 has emerged as a target for diagnosing and treating various carcinomas[11,12].

Structurally, TRPV5 and TRPV6 represent homo- or heteromeric assemblies of four subunits[13], each containing a central K^+-channel-like transmembrane domain that is flanked by intracellular amino (N)- and carboxy (C)-terminal domains. The overall architecture and potential gating mechanisms of TRP channels have recently been illuminated by cryo-electron microscopy structures of TRPV1 (refs 14, 15), TRPV2 (ref. 16) and TRPA1 (ref. 17). However, the absence of structural bases for the unique physiological properties of TRPV5 and TRPV6 motivated us to study these epithelial Ca^{2+} channels.

Structure determination

We screened various orthologues of TRPV5 and TRPV6 and discovered rat TRPV6 as a promising candidate for our structural studies. We modified the 727-residue wild-type rat TRPV6 polypeptide to create the crystallization construct $TRPV6_{cryst}$ (see Methods). Experiments with the fluorescent Ca^{2+} indicator Fura-2 AM show that cells expressing $TRPV6_{cryst}$ exhibit Ca^{2+} permeability similar to wild type (Extended Data Fig. 1).

The best crystals of $TRPV6_{cryst}$ diffracted to 3.25 Å resolution. We solved the $TRPV6_{cryst}$ structure by molecular replacement, and the electron density map (Extended Data Fig. 2) was readily interpretable for most of the polypeptide (see Methods). Sequence registry was aided by anomalous difference Fourier maps highlighting natural sulfur atoms of cysteines and methionines, and selenium atoms in protein with selenomethionines substituted for methionines (Extended Data Fig. 3). The resulting model of $TRPV6_{cryst}$ was refined to good crystallographic statistics and stereochemistry (Extended Data Table 1).

Architecture and domain organization

The four-fold symmetrical structure of $TRPV6_{cryst}$ (Fig. 1) contains two main components: a transmembrane domain with a central ion channel pore, and a ~70 Å-tall and ~110 Å-wide intracellular skirt where four subunits constitute walls enclosing a ~50 Å × 50 Å-wide cavity underneath the ion channel. Like TRPV1 (ref. 14) (Extended Data Fig. 4) and TRPV2 (ref. 16), the intracellular domains of a single $TRPV6_{cryst}$ subunit contain an ankyrin repeat domain with six ankyrin repeats, followed by a linker domain that includes a β-hairpin (composed of β-strands β1 and β2) and a helix–turn–helix motif resembling a seventh ankyrin repeat, and the pre-S1 helix, which connects the linker domain to the transmembrane domain (Fig. 1d–f and Extended Data Fig. 4). Also similar to TRPV1/2, a six-residue stretch at the C terminus constitutes a β-strand (β3) that tethers to the β-hairpin in the linker domain to create a three-stranded β-sheet. In addition to the conserved domains, $TRPV6_{cryst}$ also includes an N-terminal helix and C-terminal hook, which pack against each other to form an intersubunit interface along the corners of the intracellular skirt.

Similar to other TRP channels[14,16,17], the transmembrane domain of $TRPV6_{cryst}$ crudely resembles voltage-gated K^+ (ref. 18) or Na^+ (ref. 19) channels and includes six transmembrane helices (S1–S6) and a pore loop (P-loop) between S5 and S6. The first four transmembrane helices form a bundle to constitute the S1–S4 domain. The packing of aromatic side chains in S1–S4 rigidifies the helical bundle conformation (Extended Data Fig. 4c), suggesting that this domain remains relatively static during gating. The linker between the S1–S4 domain and pore

[1]Department of Biochemistry and Molecular Biophysics, Columbia University, 650 West 168th Street, New York, New York 10032, USA.
*These authors contributed equally to this work.

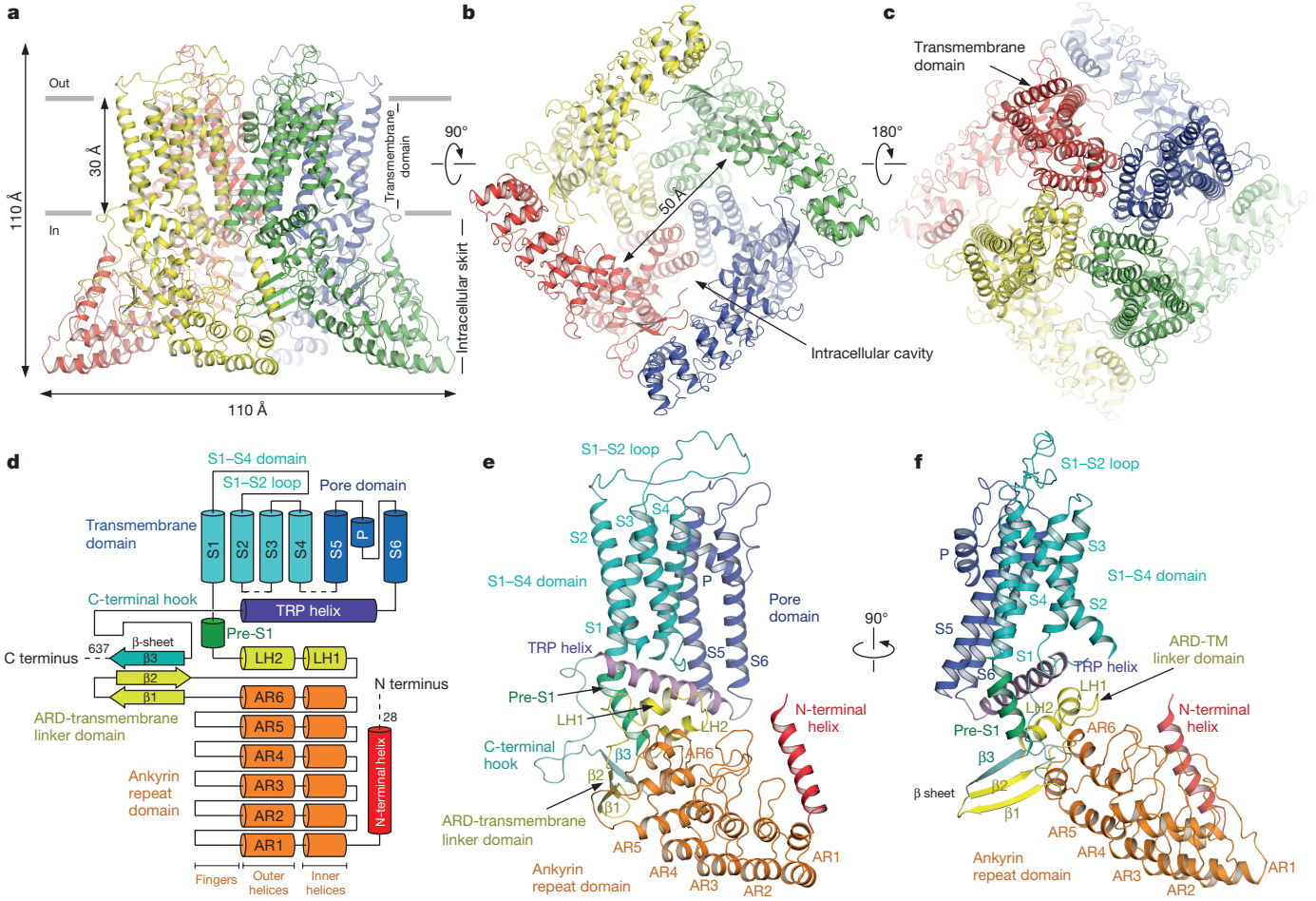

Figure 1 | Architecture and domain organization of TRPV6$_{cryst}$. **a**–**c**, Side (**a**), bottom (**b**) and top (**c**) views of the TRPV6$_{cryst}$ tetramer, with each subunit shown in a different colour. **d**, Domain organization diagram of the TRPV6 subunit. **e**, **f**, Two views of the TRPV6$_{cryst}$ subunit, with domains coloured as in **d**.

domain is unstructured, which is a marked contrast from other TRP channels, in which it assumes a helical conformation and mediates interdomain interactions[14,16,17]. Following S6 is the amphipathic TRP helix, which runs parallel to the membrane and interacts with intracellular soluble domains in a manner analogous to TRPV1, TRPV2 and TRPA1 (refs 14, 16, 17).

Although the overall domain organization of TRPV6$_{cryst}$ resembles TRPV1/2 (refs 14, 16) and, to a lesser degree, TRPA1 (ref. 17), electron density for the linker between S6 and TRP helix (Extended Data Fig. 2f) and disulfide crosslink experiments (Extended Data Fig. 5a–c) imply a unique non-swapped transmembrane domain arrangement in which the S1–S4 domain and pore domain of the same protomer are packed against each other. While this unique domain arrangement could have profound implications, we present this aspect of the TRPV6$_{cryst}$ model cautiously because of the absence of interpretable density for the S4–S5 linker.

Assembly and subunit interfaces

Assembly of TRPV6$_{cryst}$ is mediated by multiple interdomain interfaces (Fig. 2). Close packing of S5 against S4 and S1 of the adjacent S1–S4 domain immobilizes the pore module with respect to the S1–S4 domain (Fig. 2a), a trait that is reminiscent of the Slo2.2 K^+ channel[20] and distinct from voltage-gated channels[18]. Further, the S1–S2 extracellular loop contacts the S5–P and P–S6 loops (Fig. 2a). This interaction hints at a structural basis for the regulation of TRPV5 and TRPV6 function by the β-glucuronidase klotho, which modulates channel activity by modifying the conserved N-linked glycosylation site[21] located in the middle of this loop (N357 in TRPV6$_{cryst}$).

The intracellular domains of TRPV5 and TRPV6 have been implicated in tetrameric assembly[22], trafficking[23] and regulation of channel activity by the Ca^{2+} sensor calmodulin[24–26]. The structure of TRPV6$_{cryst}$ reveals that numerous non-contiguous intracellular domains engage in extensive inter- and intrasubunit interactions (Fig. 2c). At the centre of these interactions is the N-terminal helix, which is positioned as a pillar along the corners of the intracellular skirt. Putative hydrogen bonds and salt bridges involving D34 stabilize the interaction between the N-terminal helix and three-stranded β-sheet. Notably, mutation of the equivalent D34 to alanine abolished Ca^{2+} uptake function in TRPV5 (ref. 23), suggesting this interaction's functional importance. The N-terminal helix also forms hydrophobic and hydrogen bonding interactions with the C-terminal hook and pre-S1 helix from an adjacent subunit. Since it is a hub for domain interactions, endogenous or exogenous factors could allosterically modulate channel activity by targeting the N-terminal helix. Interestingly, we observed a robust cylindrical density at the intersubunit interface formed by the N-terminal helix, ankyrin repeat domain and three-stranded β-sheet (Extended Data Fig. 5d–h). We have tentatively attributed this density to desthiobiotin (DTB), which was included as an eluent in the TRPV6$_{cryst}$ affinity purification procedure (see Methods).

Ion-conducting pore

The extracellular portion of the TRPV6$_{cryst}$ ion-conducting pore is formed by extracellular loops connecting the P-loop helix to S5 and S6, while the rest of the ion conduction pathway is formed entirely by the S6 helices (Fig. 3). Such pore architecture is conserved over the entire family of tetrameric ion channels (Extended Data Fig. 6).

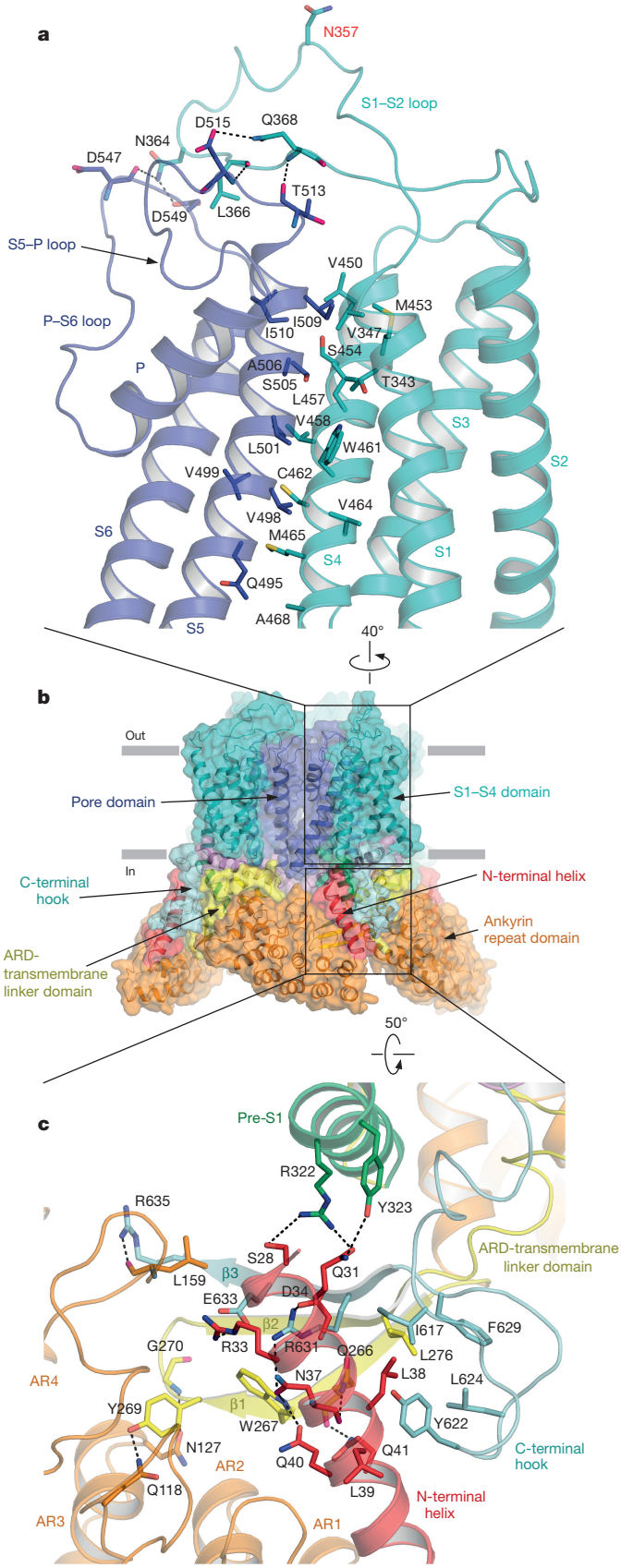

Figure 2 | Domain interfaces. a, Transmembrane helices S4 and S5 and extracellular loops S1–S2, S5–P and P–S6 contribute to interfaces between the S1–S4 domain and pore domain. **b**, Side view of the $TRPV6_{cryst}$ tetramer with domains coloured differently. Boxes indicate domain interfaces expanded in **a** and **c**. **c**, Interfaces between soluble domains. Residues at domain interfaces in **a** and **c** are shown in stick representation, with potential hydrogen bonds and electrostatic interactions shown as dashed lines. The predicted N-linked glycosylation site conserved in TRPV6 channels, N357 in $TRPV6_{cryst}$, is labelled red in **a**.

The region connecting S5 and S6 contains eight acidic residues per protomer, four of which face the ion conduction pathway to produce a highly electronegative 'mouth' to the pore (Fig. 3a–c). Below this extracellular vestibule is a four-residue selectivity filter (^{538}TIID^{541}) (Fig. 3d–f). The side chains of D541, which have previously been identified as critical for Ca^{2+} selectivity, permeation and voltage-dependent Mg^{2+} block[2], protrude towards the pore central axis to produce a minimum interatomic distance of 4.6 Å (Fig. 3f–g) at the upper tip of the selectivity filter. Three phenylalanine residues (F530, F533 and F536) in the pore helix, which are conserved in TRPV5–6, but only one of which is conserved in TRPV1–4 (Extended Data Fig. 7), may restrict its dynamics. A relatively static outer pore domain could reflect a key difference between TRPV5/6 and other TRPV channels, which gate in response to various stimuli and thus should display a higher degree of structural plasticity, as exemplified by toxin- and capsaicin-induced conformational changes in TRPV1 (ref. 15).

Below the selectivity filter, the pore widens into a large, mainly hydrophobic cavity (Fig. 3e). Lateral pore portals (Fig. 3a, b) may provide hydrophobic access to this cavity for small molecules or lipids, similar to voltage gated Na^+ channels[19]. The large diameter of the hydrophobic cavity (~13 Å) can easily accommodate a fully hydrated calcium ion, which has an effective diameter of 8–10 Å. The S6 helices cross at the intracellular portion of the channel, where the M577 side chains form the narrow constriction (5.1 Å diameter) and define the lower gate (Figs 3d–f), similar to TRPV2 (ref. 16). Importantly, anomalous diffraction from crystals grown with selenomethionine-labelled protein showed a robust signal (Fig. 3h and Extended Data Fig. 3c), confirming that M577 side chains occlude the pore. Despite high sequence conservation in this region (Extended Data Fig. 7), in TRPV1 the equivalent residue to TRPV6 M577 points away from the pore axis (Extended Data Fig. 6a).

Cation–binding sites

Previous research has resulted in the proposal that TRPV5 and TRPV6 achieve their exceptional Ca^{2+} selectivity through binding of Ca^{2+} to the selectivity filter[2]. Indeed, we observed a strong $2F_o - F_c$ density consistent with a bound ion at the central pore axis, surrounded closely by the carbonyl oxygens of D541 side chains (Extended Data Fig. 2e). Since the pore diameter here (4.6 Å, measured between centres of opposing oxygen atoms) is large enough to accommodate a dehydrated calcium ion (typical Ca^{2+}–oxygen distance is ~2.4 Å), we contend that the selectivity filter is captured in a Ca^{2+}-conducting state. To further resolve cation-binding sites in the pore, we co-crystallized $TRPV6_{cryst}$ with Ca^{2+}, Ba^{2+} or Gd^{3+}, which have various permeation and channel-blocking properties[27] (Extended Data Fig. 1) and collected X-ray diffraction data to locate anomalous difference peaks.

The anomalous difference peaks suggest the presence of four types of cation-binding site in the $TRPV6_{cryst}$ channel pore (Fig. 4). Notably, two of these (sites 1 and 2) have locations approximately equivalent to Ca^{2+} sites in the genetically engineered Ca^{2+}-selective channel Ca_VAb[28], but none of them overlap with the putative Ca^{2+} site in $Ca_V1.1$ (ref. 29) (Extended Data Fig. 6m–o). For Ba^{2+} and Gd^{3+}, four symmetry-related peaks were observed in the $TRPV6_{cryst}$ outer vestibule, in the vicinity of D517, E518 and D547 (Fig. 4c–f). Interestingly, the Ba^{2+} and Gd^{3+} sites occupy distinct locations, probably because of difference in charge density. Although these signals were not observed for $TRPV6_{cryst}$ co-crystallized with Ca^{2+} (Fig. 4a–b), presumably because of lower affinity, reduced occupancy or weaker anomalous signal, we speculate that the highly electronegative outer vestibule is involved in the general recruitment of cations towards the extracellular vestibule of

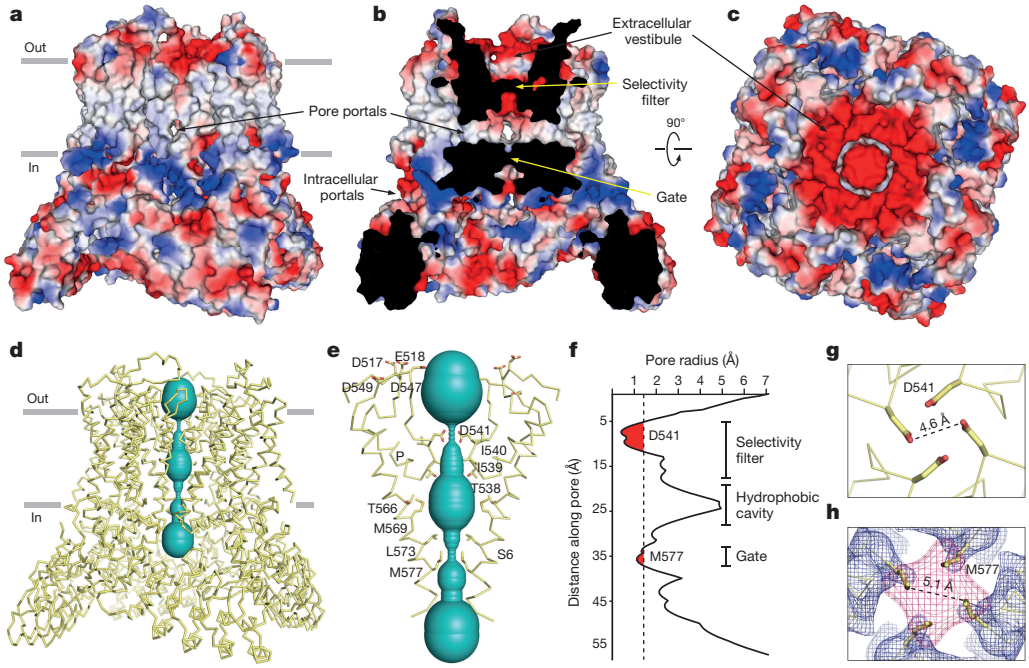

Figure 3 | Permeation pathway. a–c, Side (**a**), central slice (**b**) and top (**c**) views of TRPV6$_{cryst}$ structure in surface representation, coloured by electrostatic potential. **d**, Ribbon diagram of the TRPV6$_{cryst}$ tetramer, with ion conduction pathway shown in cyan. **e**, Expanded view of the TRPV6$_{cryst}$ pore, with front and back subunits excluded for clarity. Acidic side chains in the extracellular vestibule and pore-lining side chains are shown as sticks. **f**, Radius of the pore calculated using HOLE. D541 and M577 form narrow constrictions at the selectivity filter and intracellular gate, respectively. **g**, **h**, Top views of narrow constrictions formed by D541 (**g**) and M577 (**h**). In **h**, blue and pink mesh shows electron density for M577 ($2F_o - F_c$, 45–3.25 Å, 1.0σ) and anomalous difference electron density from selenomethione-labelled crystal (30–5.00 Å, 3.0σ), respectively.

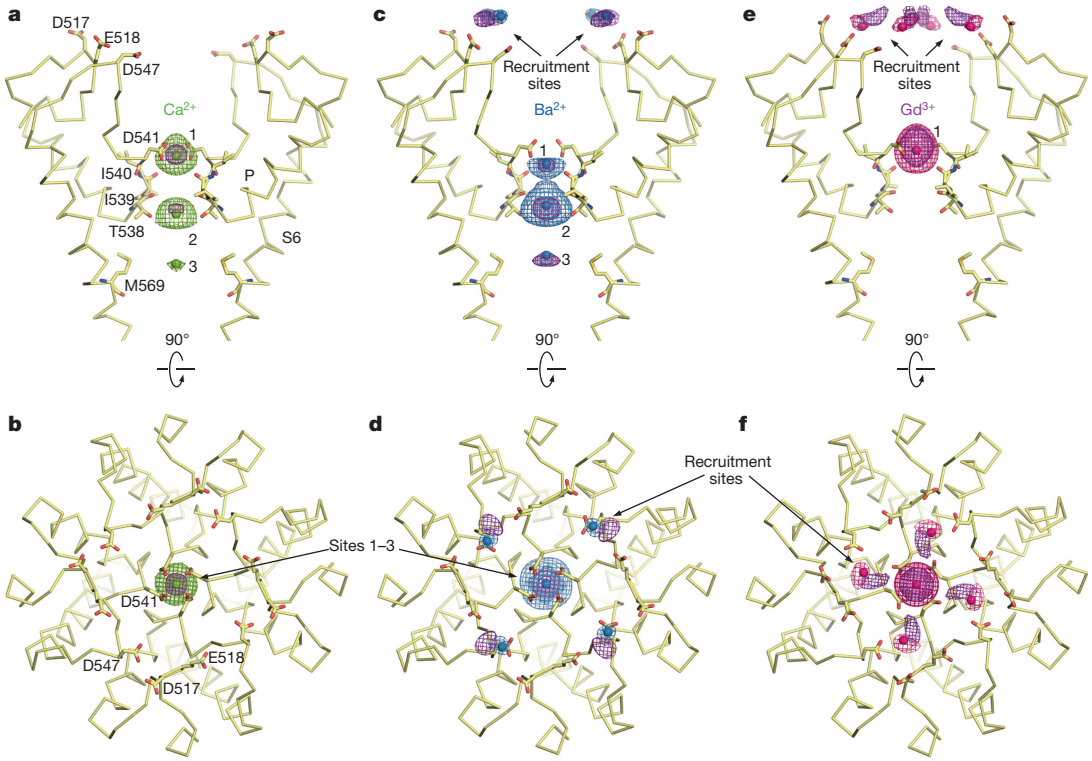

Figure 4 | Cation-binding sites in the TRPV6$_{cryst}$ pore. Side (**a**, **c**, **e**) and top (**b**, **d**, **f**) views of the TRPV6$_{cryst}$ pore, with residues important for cation binding shown in stick representation. Front and back subunits in **a**, **c** and **e** are removed for clarity. Green, blue and pink mesh shows anomalous difference electron density for Ca^{2+} (**a**, **b**, 38–4.59 Å, 2.7σ), Ba^{2+} (**c**, **d**, 38–4.59 Å, 3.5σ) and Gd^{3+} (**e**, **f**, 38–4.59 Å, 7σ), and ions are shown as spheres of the corresponding colour. Purple mesh shows simulated-annealing $F_o - F_c$ electron density maps contoured at 4σ for Ca^{2+} (50–3.65 Å), 3σ for Ba^{2+} (50–3.85 Å) and 3.5σ for Gd^{3+} (50–3.80 Å). The amplitudes of the anomalous peaks are listed in Extended Data Fig. 8c. D547 and E518 side chains are apparently involved in coordination of Ba^{2+} ions at the recruitment sites. The Gd^{3+} recruitment sites are distinct from Ba^{2+} and apparently involve coordination by D517, E518 and D547 side chains.

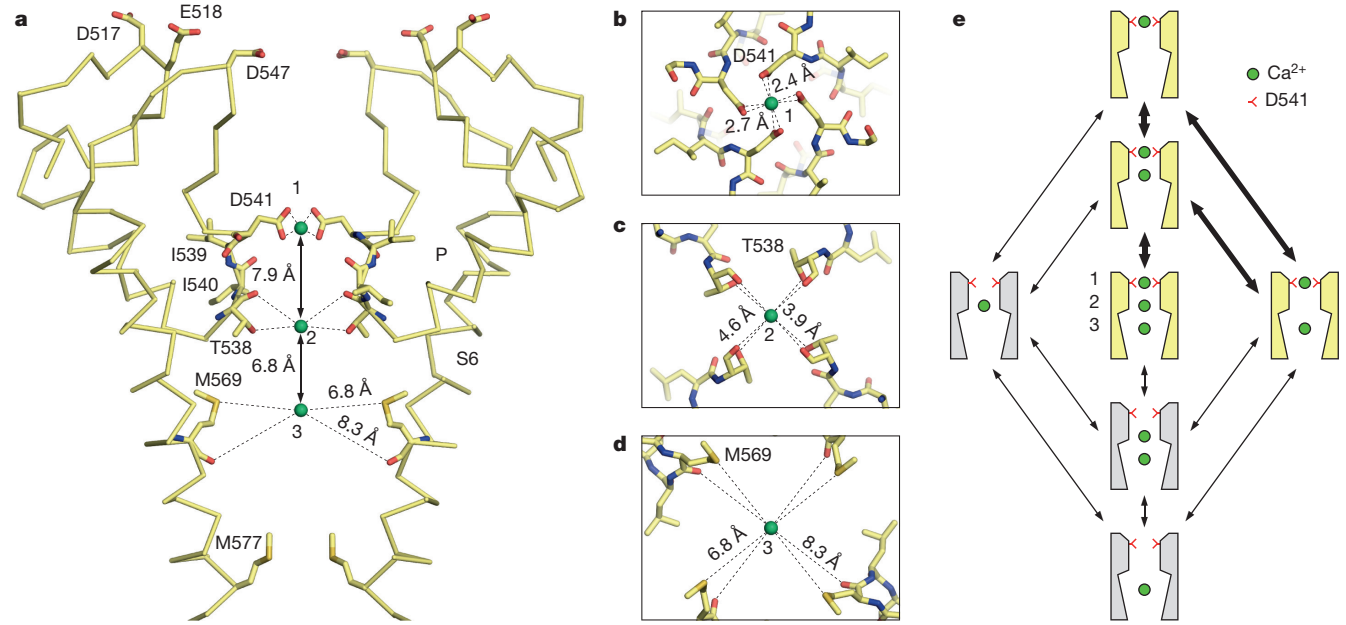

Figure 5 | Calcium permeation mechanism. a, Side view of $TRPV6_{cryst}$ pore, with front and back subunits removed for clarity. Residues that surround or contribute to cation-binding sites are shown as sticks, and Ca^{2+} ions at sites 1, 2 and 3 are shown as green spheres. **b**–**d**, Top views of Ca^{2+} ions at sites 1 (**b**), 2 (**c**) and 3 (**d**), with nearby residues shown as sticks. The interatomic distances illustrated by dashed lines suggest that Ca^{2+} is directly coordinated by D541 side chains at site 1, while a hydrated Ca^{2+} ion indirectly interacts with the pore at sites 2 and 3. **e**, Schematic representation of various Ca^{2+} occupancy states in TRPV6. Presumed lower energy states are shown in yellow, and most probable transitions are highlighted with bold arrows. Occupancy states in which site 1 is vacant (shown in grey) are likely only to be transiently populated, owing to electrostatic repulsion of D541 side chains. Sufficiently large distances between sites 1, 2 and 3 suggest that electrostatic repulsion between Ca^{2+} ions does not preclude simultaneous binding at all three sites.

the TRPV6 channel. Lower affinity of the recruitment sites compared with the main binding site in the centre of the pore for Gd^{3+} is consistent with the results of isothermal titration calorimetry experiments (Extended Data Fig. 8a, b).

The strongest anomalous difference peaks for Ca^{2+} and Gd^{3+} were observed along the central pore axis at or near the same plane as D541 side chains (Fig. 4a, b, e, f), indicating that this locus constitutes the main cation-binding site (site 1). The cation–oxygen distance of 2.4 Å (Fig. 5b) matches the reported average Ca^{2+}–oxygen distance calculated from crystal structures of various classes of Ca^{2+}-binding proteins[30]. This minimal interatomic distance suggests that the carboxylate oxygens of D541 directly coordinate an at least partly dehydrated Ca^{2+} ion at this site. Similarly, structural studies of the hexameric Ca^{2+} release-activated channel Orai suggest that Ca^{2+} selectivity is achieved by direct coordination of Ca^{2+} by a ring of glutamate residues at the extracellular entrance to the pore[31]. By contrast, in Ca_VAb, the permeant Ca^{2+} ion indirectly interacts with the pore through water molecules[28]. The presence of a robust Gd^{3+} signal at site 1 shows that trivalents can bind at D541 as well (Fig. 4e, f).

For Ca^{2+} and Ba^{2+}, an additional anomalous difference signal is observed at the centre of the pore, 6–8 Å below site 1, between the backbone carbonyls and side-chain hydroxyl groups of T538 (site 2). The greater Ca^{2+}/Ba^{2+}–oxygen distance at site 2 (~4 Å, Figs 4a, c and 5c) indicates that the cation is equatorially hydrated at this location. Although the chemical environment of site 2 suggests that it binds cations at lower affinity than site 1, the Ba^{2+} signal is stronger at this site (Extended Data Fig. 8c). The different relative anomalous peak intensities of sites 1 and 2 for Ca^{2+} and Ba^{2+}, as well as their slightly different positions at site 1, may arise from the greater size of Ba^{2+} (~3 Å diameter) than Ca^{2+} (~2 Å diameter). This observation implies that the TRPV6 selectivity filter discriminates ions on the basis of size as well as charge.

Anomalous difference peaks were observed for Ca^{2+} and Ba^{2+} 6.8 Å below site 2 in the centre of the hydrophobic cavity, at the level of M569 (site 3) (Figs 4a, c and 5a, d). For Ca^{2+}, the anomalous peak at site 3 is less robust (Extended Data Fig. 8c), presumably because of weaker anomalous diffraction properties. The signal at site 3 suggests that cations bound here are ordered by water molecules, which can be held in place by weak hydrogen bonding interactions and pore helix dipoles pointing their partial negative charges towards the centre of the hydrophobic cavity.

Mechanism of ion permeation

The pore architecture and locations of cation-binding sites in the $TRPV6_{cryst}$ structure (Fig. 5a–d) illuminate a potential calcium permeation mechanism (Fig. 5e). The close proximity of carboxylate side chains at site 1 suggests that, in the present pore conformation, the absence of a bound Ca^{2+} ion would be energetically unfavourable because of charge repulsion between D541 side chains. Thus, it is likely that a Ca^{2+} ion is, in effect, constitutively bound at site 1 and removal of a Ca^{2+} ion from site 1 would require immediate replacement with another Ca^{2+} ion, necessitating a 'knock-off' mechanism of permeation similar to the genetically engineered Ca^{2+}-selective channel Ca_VAb[28]. Given the large energetic barrier of displacing a Ca^{2+} ion at site 1, a substantially high local concentration of Ca^{2+} would be necessary for permeation to proceed at physiological membrane voltages. Recruitment sites in the highly electronegative extracellular vestibule might serve this purpose.

As direct coordination by aspartate side chains suggests that site 1 is the highest affinity site for Ca^{2+} in TRPV6 channel pore, knock-off from site 1 is likely to be the rate-limiting step for Ca^{2+} permeation. After the Ca^{2+} ion is knocked off site 1, it moves towards site 2, where it is coordinated through its hydration shell by the backbone carbonyls and sidechain hydroxyls of T538. In Ca_vAb[28], Ca^{2+} also binds in the middle of the selectivity filter, at a locus between site 1 and site 2 of $TRPV6_{cryst}$ (Extended Data Fig. 6m, n). Although we found no crystallographic evidence for Ca^{2+} bound at an equivalent site in $TRPV6_{cryst}$, it is plausible that such a site is occupied transiently during stepwise Ca^{2+} permeation. Whether a knock-off is necessary for the Ca^{2+} ion to traverse from site 2 to site 3 is unclear, as electrostatic repulsion

between Ca^{2+} ions at site 1 and site 2 (and possibly, the aforementioned site between sites 1 and 2) may contribute a driving force. At site 3, the Ca^{2+} ion is poised to enter the cell. Since the lower gate is closed in the current $TRPV6_{cryst}$ structure, further studies are necessary to elucidate whether its opening affects cation binding in the pore.

Previous observations have suggested that, in addition to Ca^{2+}, TRPV6 is permeable to other divalents (with ion permeation sequence $Ca^{2+} > Sr^{2+} \approx Ba^{2+} > Mn^{2+}$)[4] and weakly to trivalents (La^{3+} and Gd^{3+})[27] as well. The anomalous difference peaks for Ba^{2+} and Gd^{3+} indicate that the permeation mechanism of other cations differs from Ca^{2+} permeation to varying degrees. Ba^{2+}, for example, apparently has a stronger anomalous electron density at site 2 (Extended Data Fig. 8c), which suggests a higher affinity for that site than site 1. Thus, knock-off of Ba^{2+} from site 2 to site 3 may be slower and more rate-limiting than knock-off from site 1 to site 2. Larger and more positively charged ions such as Gd^{3+} may permeate differently from divalent cations, since their high charge density may preclude simultaneous binding at sites 1 and 2. Nevertheless, trivalents probably block divalents from permeating by virtue of their strong positive charge, which results in higher affinity binding at site 1. Likewise, Ca^{2+} and Mg^{2+} probably block monovalent currents[2] through an analogous mechanism. Further studies will be necessary to elucidate the intricate details of cation permeation and selectivity in epithelial Ca^{2+} channels.

Online Content Methods, along with any additional Extended Data display items and Source Data, are available in the online version of the paper; references unique to these sections appear only in the online paper.

Received 14 January; accepted 6 April 2016.
Published online 13 June 2016.

1. Clapham, D. E. TRP channels as cellular sensors. *Nature* **426,** 517–524 (2003).
2. Owsianik, G., Talavera, K., Voets, T. & Nilius, B. Permeation and selectivity of TRP channels. *Annu. Rev. Physiol.* **68,** 685–717 (2006).
3. Miura, S., Sato, K., Kato-Negishi, M., Teshima, T. & Takeuchi, S. Fluid shear triggers microvilli formation via mechanosensitive activation of TRPV6. *Nature Commun.* **6,** 8871 (2015).
4. den Dekker, E., Hoenderop, J. G. J., Nilius, B. & Bindels, R. J. M. The epithelial calcium channels, TRPV5 & TRPV6: from identification towards regulation. *Cell Calcium* **33,** 497–507 (2003).
5. Woudenberg-Vrenken, T. E. *et al.* Functional TRPV6 channels are crucial for transepithelial Ca^{2+} absorption. *Am. J. Physiol. Gastrointest. Liver Physiol.* **303,** G879–G885 (2012).
6. Bianco, S. D. *et al.* Marked disturbance of calcium homeostasis in mice with targeted disruption of the Trpv6 calcium channel gene. *J. Bone Miner. Res.* **22,** 274–285 (2007).
7. Weissgerber, P. *et al.* Male fertility depends on Ca^{2+} absorption by TRPV6 in epididymal epithelia. *Sci. Signal.* **4,** ra27 (2011).
8. Fecher-Trost, C., Weissgerber, P. & Wissenbach, U. in *Mammalian Transient Receptor Potential (TRP) Cation Channels* (eds Nilius, B. & Flockerzi, V.) Ch. TRPV6 Channels, 359–384 (Springer, 2014).
9. Lehen'kyi, V., Raphaël, M. & Prevarskaya, N. The role of the TRPV6 channel in cancer. *J. Physiol. (Lond.)* **590,** 1369–1376 (2012).
10. Raphaël, M. *et al.* TRPV6 calcium channel translocates to the plasma membrane via Orai1-mediated mechanism and controls cancer cell survival. *Proc. Natl Acad. Sci. USA* **111,** E3870–E3879 (2014).
11. Bowen, C. V. *et al. In vivo* detection of human TRPV6-rich tumors with anti-cancer peptides derived from soricidin. *PLoS ONE* **8,** e58866 (2013).
12. Bolanz, K. A., Kovacs, G. G., Landowski, C. P. & Hediger, M. A. Tamoxifen inhibits TRPV6 activity via estrogen receptor-independent pathways in TRPV6-expressing MCF-7 breast cancer cells. *Mol. Cancer Res.* **7,** 2000–2010 (2009).
13. Hoenderop, J. G. J. *et al.* Homo- and heterotetrameric architecture of the epithelial Ca^{2+} channels TRPV5 and TRPV6. *EMBO J.* **22,** 776–785 (2003).
14. Liao, M., Cao, E., Julius, D. & Cheng, Y. Structure of the TRPV1 ion channel determined by electron cryo-microscopy. *Nature* **504,** 107–112 (2013).
15. Cao, E., Liao, M., Cheng, Y. & Julius, D. TRPV1 structures in distinct conformations reveal activation mechanisms. *Nature* **504,** 113–118 (2013).
16. Zubcevic, L. *et al.* Cryo-electron microscopy structure of the TRPV2 ion channel. *Nature Struct. Mol. Biol.* **23,** 180–186 (2016).
17. Paulsen, C. E., Armache, J. P., Gao, Y., Cheng, Y. & Julius, D. Structure of the TRPA1 ion channel suggests regulatory mechanisms. *Nature* **520,** 511–517 (2015).
18. Long, S. B., Tao, X., Campbell, E. B. & MacKinnon, R. Atomic structure of a voltage-dependent K^+ channel in a lipid membrane-like environment. *Nature* **450,** 376–382 (2007).
19. Payandeh, J., Scheuer, T., Zheng, N. & Catterall, W. A. The crystal structure of a voltage-gated sodium channel. *Nature* **475,** 353–358 (2011).
20. Hite, R. K. *et al.* Cryo-electron microscopy structure of the Slo2.2 Na^+-activated K^+ channel. *Nature* **527,** 198–203 (2015).
21. Lu, P., Boros, S., Chang, Q., Bindels, R. J. & Hoenderop, J. G. The β-glucuronidase klotho exclusively activates the epithelial Ca^{2+} channels TRPV5 and TRPV6. *Nephrol. Dial. Transplant.* **23,** 3397–3402 (2008).
22. Chang, Q. *et al.* Molecular determinants in TRPV5 channel assembly. *J. Biol. Chem.* **279,** 54304–54311 (2004).
23. de Groot, T. *et al.* Role of the transient receptor potential vanilloid 5 (TRPV5) protein N terminus in channel activity, tetramerization, and trafficking. *J. Biol. Chem.* **286,** 32132–32139 (2011).
24. Cao, C., Zakharian, E., Borbiro, I. & Rohacs, T. Interplay between calmodulin and phosphatidylinositol 4,5-bisphosphate in Ca^{2+}-induced inactivation of transient receptor potential vanilloid 6 channels. *J. Biol. Chem.* **288,** 5278–5290 (2013).
25. Lambers, T. T., Weidema, A. F., Nilius, B., Hoenderop, J. G. J. & Bindels, R. J. M. Regulation of the mouse epithelial Ca^{2+} channel TRPV6 by the Ca^{2+}-sensor calmodulin. *J. Biol. Chem.* **279,** 28855–28861 (2004).
26. de Groot, T. *et al.* Molecular mechanisms of calmodulin action on TRPV5 and modulation by parathyroid hormone. *Mol. Cell. Biol.* **31,** 2845–2853 (2011).
27. Kovacs, G. *et al.* Heavy metal cations permeate the TRPV6 epithelial cation channel. *Cell Calcium* **49,** 43–55 (2011).
28. Tang, L. *et al.* Structural basis for Ca^{2+} selectivity of a voltage-gated calcium channel. *Nature* **505,** 56–61 (2014).
29. Wu, J. P. *et al.* Structure of the voltage-gated calcium channel $Ca_v1.1$ complex. *Science* **350,** 1492–1501 (2015).
30. Yang, W., Lee, H. W., Hellinga, H. & Yang, J. J. Structural analysis, identification, and design of calcium-binding sites in proteins. *Proteins* **47,** 344–356 (2002).
31. Hou, X., Pedi, L., Diver, M. M. & Long, S. B. Crystal structure of the calcium release-activated calcium channel Orai. *Science* **338,** 1308–1313 (2012).

Acknowledgements We thank E. C. Twomey and J. M. Sampson for comments on the manuscript, members of the E. C. Greene laboratory for assistance with their fluorimeter, and the Columbia Protein Core facility for assistance with isothermal titration calorimetry (ITC) measurements. We also thank the personnel at beamlines 24-ID-C/E of APS, X25/X29 of NSLS and 5.0.1/5.0.2 of ALS. This work was supported by National Institutes of Health grants R01 NS083660 (A.I.S.) and T32 GM008281 (K.S.), by a Pew Scholar Award in Biomedical Sciences, a Schaefer Research Scholar Award, a Klingenstein Fellowship Award in the Neurosciences and an Irma T. Hirschl Career Scientist Award (A.I.S.).

Author Contributions K.S., A.K.S., M.V.Y. and A.I.S. designed the project. K.S., A.K.S. and M.V.Y. performed the experiments. K.S., A.K.S., M.V.Y. and A.I.S. wrote the manuscript.

Author Information The structure coordinates have been deposited in Protein Data Bank (PDB) with accession numbers 5IWK, 5IWP, 5IWR and 5IWT for native, Ca^{2+}, Ba^{2+} and Gd^{3+} data, respectively. Reprints and permissions information is available at www.nature.com/reprints. The authors declare no competing financial interests. Readers are welcome to comment on the online version of the paper. Correspondence and requests for materials should be addressed to A.I.S. (as4005@cumc.columbia.edu).

METHODS

No statistical methods were used to predetermine sample size. The experiments were not randomized. The investigators were not blinded to allocation during experiments and outcome assessment.

Constructs. Using fluorescence-detection size-exclusion chromatography (FSEC)[32], we screened numerous TRPV5 and TRPV6 orthologues fused to enhanced green fluorescent protein (eGFP)[33] at the C terminus and identified rat TRPV6 (GenBank EDM15484.1) as the best candidate for crystallographic trials. The fortuitous spontaneous mutation L495Q generated during gene synthesis was found to increase expression level of rat TRPV6. C-terminal truncation mutants of rat TRPV6-L495Q produced crystals in the *C*222 space group that diffracted to ~6 Å resolution. On the basis of an initial low-resolution molecular replacement solution, we designed numerous mutations aimed at improving crystal packing, including individual substitutions of surface residues, fusions with soluble protein partners and flexible loop deletions. Incorporation of the surface residue mutations L92N and M96Q helped improve the resolution limit of crystals in the *C*222 space group to ~4.0 Å. Further screening of surface residue mutations yielded the amino-acid substitution I62Y, which facilitated crystallization in the $P42_12$ space group and improved diffraction resolution to 3.25 Å. Inspection of protein-mediated crystal contacts in this crystal form shows that cation-π and/or hydrogen-bonding interactions involving the side chains of I62Y, K63, K66 and F67 might have permitted crystallization in the $P42_12$ space group and contributed to the improved resolution (Extended Data Fig. 9). The final construct, $TRPV6_{cryst}$, comprises residues 1–668 and contains the point mutations I62Y, L92N, M96Q and L495Q.

Expression and purification. $TRPV6_{cryst}$ was introduced into a pEG BacMam vector[34] with C-terminal thrombin cleavage site (LVPRG) followed by eGFP and streptavidin affinity tag (WSHPQFEK). Baculovirus was made in Sf9 cells (Thermo Fisher Scientific, mycoplasma test negative). For large-scale expression, suspension-adapted HEK 293S cells lacking *N*-acetyl-glucosaminyltransferase I (GnTI) (ATCC, mycoplasma test negative) were grown in Freestyle 293 media (Life Technologies) supplemented with 2% FBS at 37 °C in the presence of 5% CO_2. The culture was transduced with P2 baculovirus once cells reached a density of 2.5×10^6 to 3.5×10^6 per millilitre. After 8–12 h, 10 mM sodium butyrate was added and the temperature was changed to 30 °C. Cells were harvested 48–72 h after transduction and resuspended in a buffer containing 150 mM NaCl, 20 mM Tris-HCl pH 8.0, 1 mM β-mercaptoethanol (βME), 0.8 μM aprotinin, 2 μg ml^{-1} leupeptin, 2 mM pepstatin A and 1 mM phenylmethysulfonyl fluoride (PMSF). The cells were disrupted using a Misonix Sonicator (12 × 15 s, power level 7), and the resulting homogenate was clarified using a Sorval centrifuge at 9,900*g* for 15 min. Crude membranes were collected by ultracentrifugation for 1 h in a Beckman Ti45 rotor at 186,000*g*. The membranes were mechanically homogenized and subsequently solubilized for 2–4 h in a buffer containing 150 mM NaCl, 20 mM Tris-HCl pH 8.0, 1 mM βME, 20 mM *n*-dodecyl-β-D-maltopyranoside (DDM), 0.8 μM aprotinin, 2 μg ml^{-1} leupeptin, 2 mM pepstatin A and 1 mM PMSF. After insoluble material was removed by ultracentrifugation, streptavidin-linked resin was added to the supernatant and rotated for 4–16 h. Resin was washed with 10 column volumes of wash buffer containing 150 mM NaCl, 20 mM Tris pH 8.0, 1 mM βME and 1 mM DDM, and the protein was eluted using wash buffer supplemented with 2.5 mM D-desthiobiotin. The eluted fusion protein was concentrated to ~1.0 mg ml^{-1} and digested with thrombin at a mass ratio of 1:100 (thrombin:protein) for 1.5 h at 22 °C. The digested protein was concentrated and injected into a Superose 6 column equilibrated in a buffer composed of 150 mM NaCl, 20 mM Tris-HCl pH 8.0, 1 mM βME and 0.5 mM DDM. Tris(2-carboxyethyl)phosphine (TCEP; 10 mM) was added to fractions with elution time corresponding to the tetrameric channel, and protein was concentrated to 2.5–3.0 mg ml^{-1} using a 100 kDa MWCO concentrator. All purification steps were conducted on ice or at 4 °C. Typical purifications yielded ~1 mg of purified protein per litre of transduced cells.

Protocols to express selenomethionine-labelled protein in HEK cells were adapted from literature[35]. Six to 8 h after transduction, cells were pelleted and resuspended in DMEM (Life Technologies) supplemented with 10% FBS and lacking L-methionine. After shaking methionine-depleted cells for 6 h at 37 °C, 60 mg of L-selenomethionine was added per litre of cells. Thirty-six to 48 h after transduction, cells were harvested and protein was purified using the same protocol as described above, except for the addition of 4 mM L-methionine to all purification buffers, excluding the final gel filtration buffer. This procedure yielded ~0.4 mg of selenomethionine-labelled protein per litre of transduced cells.

Crystallization and structure determination. Initial high-throughput vapour diffusion crystallization screens showed that purified $TRPV6_{cryst}$ crystallizes in numerous conditions containing low molecular mass polyethylene glycols (PEG 300, PEG 350 monomethyl ether (MME), PEG 400 or PEG 550 MME). The best crystals were grown using a reservoir solution consisting of 20–24% PEG 350 MME, 100 mM NaCl and 100 mM Tris-HCl pH 8.0–8.5. To increase crystal size, 50 mM ammonium formate was added to the protein immediately before crystallization. Two microlitres of protein were mixed with 1.0–1.2 μl of reservoir solution, and incubated at 20 °C in hanging-drop vapour diffusion trays. Crystals grew as thin plates and reached full size (~400 μm × ~120 μm × ~20 μm) within 2 weeks. Crystals were cryoprotected by incubating for a short time in a solution containing 33–36% PEG 350 MME, 100 mM NaCl, 100 mM Tris-HCl pH 8.2, 0.5 mM DDM and 50 mM ammonium formate, and flash frozen in liquid nitrogen. To obtain crystals with Ca^{2+}, Ba^{2+} or Gd^{3+}, protein was incubated with 10 mM $CaCl_2$, 10 mM $BaCl_2$ or 1 mM $GdCl_3$, respectively, for at least 1 h at 4 °C before crystallization. Crystals of selenomethionine-labelled protein were grown and cryoprotected using the same procedure as crystals of native protein.

Diffraction data collected at APS (beamlines 24-ID-C/E), NSLS (beamlines X25 or X29) or ALS (beamlines 5.0.1 or 5.0.2) were processed using XDS[36] or HKL2000 (ref. 37). The initial structural solution was obtained by molecular replacement using Phaser[38] and the structure of mouse TRPV6 ankyrin domain (PDB accession number 2RFA)[39] as a search probe and the rest of the molecule was iteratively built using rat TRPV1 structure (PDB accession number 3J5P)[14] as a guide. The model encompasses most of the polypeptide (residues 27–637), excluding parts of the S2–S3 linker (residues 409–416) and S4–S5 linker (residues 471–479), which were not clearly visible in the electron density map. The model was refined by alternating cycles of building in COOT[40] and automatic refinement in Phenix[41] or Refmac[42]. Correct sequence registry was aided by anomalous difference Fourier maps calculated from crystals grown in the presence of 10 mM Ca^{2+} to highlight sulfur atoms of cysteines and methionines, and from crystals labelled with selenomethionine to highlight selenium atoms (Extended Data Fig. 3). To confirm sequence registry in the C-terminal region, where native methionines are absent, selenomethionine-labelled crystals were produced for protein containing a methionine substitution at L630 (L630M). The anomalous difference Fourier maps were calculated from X-ray diffraction data collected at 1.75 Å for Ca^{2+} and Ba^{2+}, 1.56 Å for Gd^{3+} and 0.979 Å for selenium. All structural figures were prepared in PyMol[43]. Surface representation of the ion permeation pathway was generated using the PyMol plugin version of Caver[44]. The pore radius was calculated using HOLE[45].

Fura-2 AM measurements. Wild-type rat TRPV6 or $TRPV6_{cryst}$ fused to C-terminal strep tag was expressed in HEK cells as described above. Forty-eight to 72 h after transduction, cells were harvested by centrifugation at 600*g* for 5 min. The cells were resuspended in pre-warmed modified HBS (118 mM NaCl, 4.8 mM KCl, 1 mM $MgCl_2$, 5 mM D-glucose, 10 mM HEPES pH 7.4) containing 5 μg ml^{-1} of Fura-2 AM (Life Technologies) and incubated at 37 °C for 45 min. The loaded cells were then centrifuged for 5 min at 600*g*, and resuspended in pre-warmed, modified HBS and incubated again at 37 °C for 20–30 min in the dark. The cells were subsequently pelleted and washed twice, then resuspended in modified HBS for experiments. The cells were kept on ice in the dark for maximum of ~2 h before fluorescence measurements, which were conducted using a QuantaMaster 40 spectrofluorometer (Photon Technology International) at ~25 °C in a quartz cuvette under constant stirring. Intracellular Ca^{2+} was measured by taking the ratio of two excitation wavelengths (340 and 380 nm) at one emission wavelength (510 nm). The excitation wavelength was switched at 1-s intervals.

Isothermal titration calorimetry experiments. To study the energetics of Gd^{3+} binding, we performed ITC experiments. For these, we used a MicroCal Auto-iTC200 (Malvern Instruments) instrument at the Columbia University ITC Facility. Wild-type TRPV6 protein was purified in buffer containing 20 mM Tris, 150 mM NaCl, 1 mM DDM and 1 mM βME (buffer A), and the same buffer A was also used to dissolve the desired concentrations of Gd^{3+} to avoid buffer mismatch. The experiments were performed at 25 °C using 2-μl volume injections for the titration and 700 rpm stirring speed for mixing the reactants. The experiments were performed by titrating 700 μM Gd^{3+} (by robotically controlled syringe) to 6.38-μM TRPV6 (in cell) at 3-min intervals. The control experiments were performed to calculate the heat of dilution for each injection by injecting the same volumes of Gd^{3+} into buffer A. The data were analysed using a specialized program in Origin (MicroCal ITC).

Cysteine crosslinking experiments. For SDS–PAGE and FSEC analysis, cysteine substitutions were introduced into the $TRPV6_{cryst}$ background with five exposed cysteines mutated to alanine or serine (C14S, C20S, C70A, C610A and C618A), and the surface mutation I62Y was reverted to the native isoleucine. Cysteine-substituted mutants with C-terminal eGFP and streptavidin affinity tag were expressed in HEK cells in the same way as protein for crystallization and purified with a modified protocol. Crude cell pellets were resuspended in buffer containing 150 mM NaCl, 20 mM Tris-HCl pH 8.0, 1 mM βME, 20 mM DDM, 0.8 μM aprotinin, 2 μg ml^{-1} leupeptin, 2 mM pepstatin A, 1 mM PMSF and stirred for 1–3 h. After insoluble material was removed by ultracentrifugation, streptavidin-linked resin was added to the supernatant and rotated for 4–16 h. Further steps were

performed in an identical manner to protein purification for crystallization as described above, with the exceptions that the final gel filtration buffer lacked βME, and TCEP was not added to purified protein. Within 24 h of purification, the protein samples were run on a 4–20% SDS–PAGE and visualized by Coomassie blue staining. A small portion of protein was subjected to FSEC analysis[32].

32. Kawate, T. & Gouaux, E. Fluorescence-detection size-exclusion chromatography for precrystallization screening of integral membrane proteins. *Structure* **14,** 673–681 (2006).
33. Cormack, B. P., Valdivia, R. H. & Falkow, S. FACS-optimized mutants of the green fluorescent protein (GFP). *Gene* **173,** 33–38 (1996).
34. Goehring, A. *et al.* Screening and large-scale expression of membrane proteins in mammalian cells for structural studies. *Nature Protocols* **9,** 2574–2585 (2014).
35. Barton, W. A., Tzvetkova-Robev, D., Erdjument-Bromage, H., Tempst, P. & Nikolov, D. B. Highly efficient selenomethionine labeling of recombinant proteins produced in mammalian cells. *Protein Sci.* **15,** 2008–2013 (2006).
36. Kabsch, W. Xds. *Acta Crystallogr. D* **66,** 125–132 (2010).
37. Otwinowski, Z. & Minor, W. Processing of X-ray diffraction data collected in oscillation mode. *Methods Enzymol.* **276,** 307–326 (1997).
38. McCoy, A. J. Solving structures of protein complexes by molecular replacement with Phaser. *Acta Crystallogr. D* **63,** 32–41 (2007).
39. Phelps, C. B., Huang, R. J., Lishko, P. V., Wang, R. R. & Gaudet, R. Structural analyses of the ankyrin repeat domain of TRPV6 and related TRPV ion channels. *Biochemistry* **47,** 2476–2484 (2008).
40. Emsley, P. & Cowtan, K. Coot: model-building tools for molecular graphics. *Acta Crystallogr. D* **60,** 2126–2132 (2004).
41. Adams, P. D. *et al.* PHENIX: a comprehensive Python-based system for macromolecular structure solution. *Acta Crystallogr. D* **66,** 213–221 (2010).
42. Murshudov, G. N. *et al.* REFMAC5 for the refinement of macromolecular crystal structures. *Acta Crystallogr. D* **67,** 355–367 (2011).
43. DeLano, W. L. *The PyMol Molecular Graphics System* (DeLano Scientific, 2002).
44. Chovancova, E. *et al.* CAVER 3.0: a tool for the analysis of transport pathways in dynamic protein structures. *PLoS Comput. Biol.* **8,** e1002708 (2012).
45. Smart, O. S., Neduvelil, J. G., Wang, X., Wallace, B. A. & Sansom, M. S. HOLE: a program for the analysis of the pore dimensions of ion channel structural models. *J. Mol. Graph.* **14,** 354–360, 376 (1996).
46. Derler, I. *et al.* Dynamic but not constitutive association of calmodulin with rat TRPV6 channels enables fine tuning of Ca^{2+}-dependent inactivation. *J. Physiol. (Lond.)* **577,** 31–44 (2006).
47. Lishko, P. V., Procko, E., Jin, X., Phelps, C. B. & Gaudet, R. The ankyrin repeats of TRPV1 bind multiple ligands and modulate channel sensitivity. *Neuron* **54,** 905–918 (2007).
48. Phelps, C. B., Wang, R. R., Choo, S. S. & Gaudet, R. Differential regulation of TRPV1, TRPV3, and TRPV4 sensitivity through a conserved binding site on the ankyrin repeat domain. *J. Biol. Chem.* **285,** 731–740 (2010).

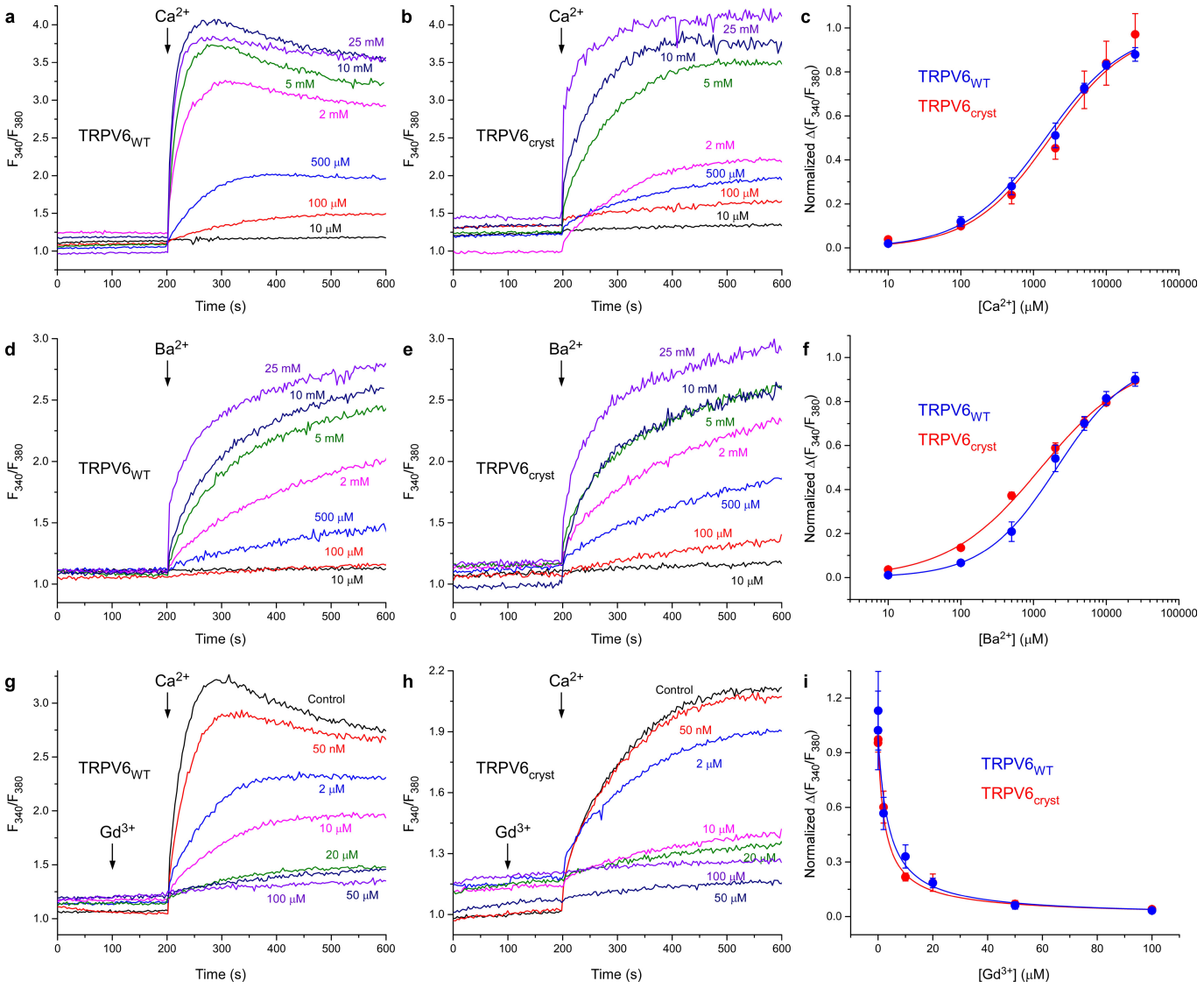

Extended Data Figure 1 | Functional characterization of wild-type rat TRPV6 and TRPV6$_{cryst}$. **a**, **b**, **d**, **e**, **g**, **h**, Representative ratiometric fluorescence measurements for HEK cells expressing wild-type rat TRPV6 (**a**, **d**, **g**) or TRPV6$_{cryst}$ (**b**, **e**, **h**). Arrows indicate the time at which the corresponding ion was added. After resuspending the cells in nominally calcium-free buffer, addition of Ca^{2+} (**a**, **b**) or Ba^{2+} (**d**, **e**) resulted in robust concentration-dependent increase in Fura-2 signal for both wild-type rat TRPV6 and TRPV6$_{cryst}$. In contrast, pre-incubation of cells with increasing concentrations of Gd^{3+} resulted in concentration-dependent reduction in Fura-2 signal for both wild type (**g**) and TRPV6$_{cryst}$ (**h**), consistent with Gd^{3+} inhibition of wild-type TRPV6 demonstrated previously using $^{45}Ca^{2+}$ uptake measurements[27]. **c**–**f**, Dose–response curves for Ca^{2+} (**c**) and Ba^{2+} (**f**) permeation calculated for wild type (blue) and TRPV6$_{cryst}$ (red) ($n = 3$ for all measurements). The changes in the fluorescence intensity ratio at 340 and 380 nm (F_{340}/F_{380}) were normalized to their approximated maximal values at saturating concentrations of Ca^{2+} or Ba^{2+}, respectively. The apparent values of half-maximum effective concentration (EC_{50}) for TRPV6$_{cryst}$ (1.70 ± 0.26 mM for Ca^{2+} and 1.27 ± 0.67 mM for Ba^{2+}) are similar to wild type (1.47 ± 0.80 mM for Ca^{2+} and 1.91 ± 0.74 mM for Ba^{2+}). **i**, Dose–response curves for Gd^{3+} inhibition calculated for wild type (blue) and TRPV6$_{cryst}$ (red) ($n = 3$ for all measurements). The changes F_{340}/F_{380} evoked by addition of 2 mM Ca^{2+} after pre-incubation with various concentrations of Gd^{3+} were normalized to the maximal change in F_{340}/F_{380} after addition of 2 mM Ca^{2+} in the absence of Gd^{3+}. The apparent values of half-maximum inhibitory concentration (IC_{50}) for wild type (3.87 ± 0.83 µM) are comparable to TRPV6$_{cryst}$ (2.57 ± 0.28 µM). Overall, the mutations introduced to crystallize TRPV6 did not significantly alter its cation permeation and inhibition properties. The absence of time-dependent decay of the Fura-2 AM signal in the case of TRPV6$_{cryst}$ is presumably due to its C-terminal truncation, which eliminated a calmodulin-binding site involved in Ca^{2+}-dependent inactivation of TRPV6 (ref. 46). Error bars, s.e.m.

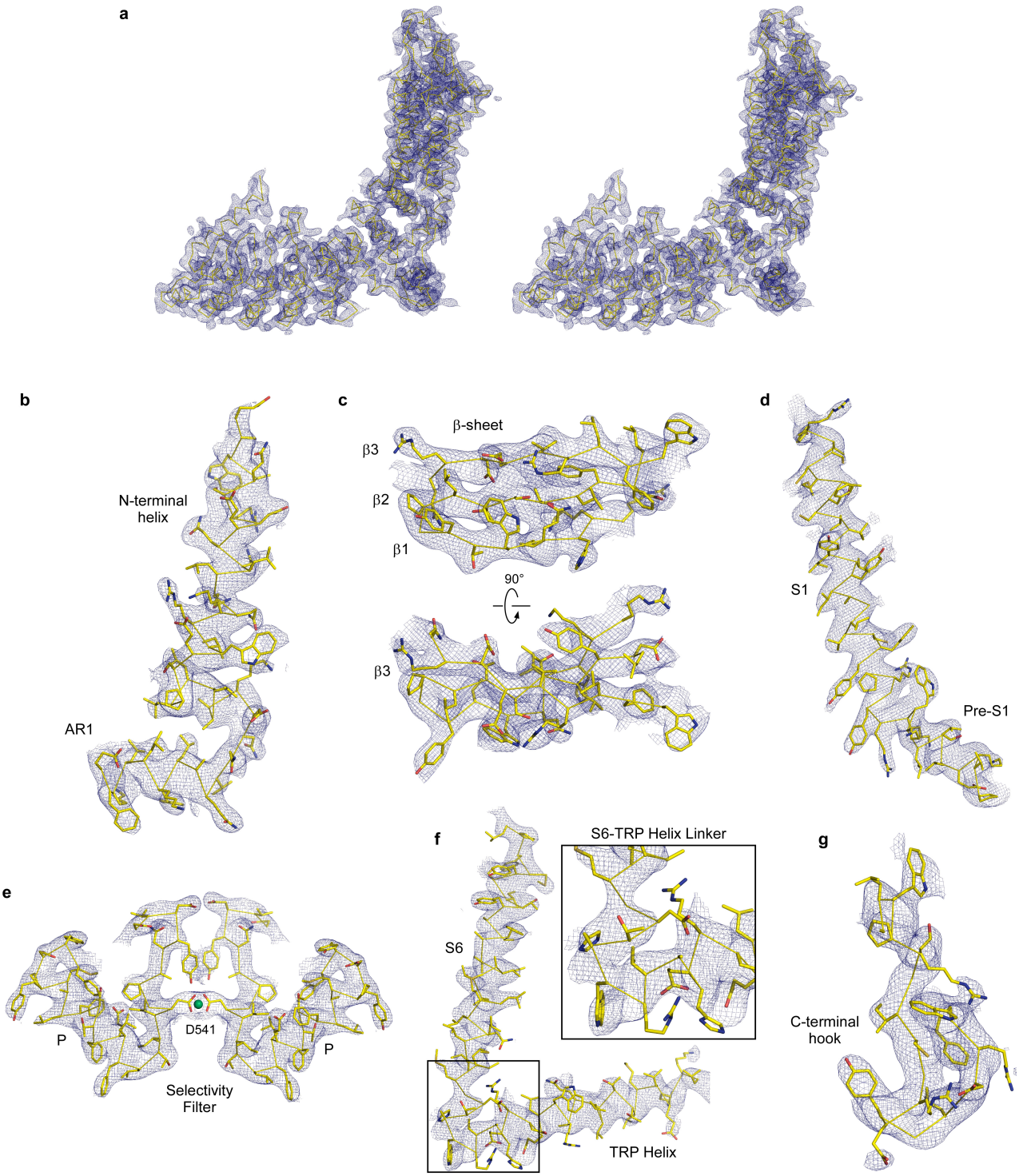

Extended Data Figure 2 | Electron density. a, Stereo view of $2F_o - F_c$ electron density map (blue mesh, 45–3.25 Å, 1.0σ) superimposed onto a ribbon model for the entire $TRPV6_{cryst}$ monomer. **b**–**g**, Close-up views of the $2F_o - F_c$ map for various portions of $TRPV6_{cryst}$ model, with side chains shown in stick representation. In **e**, two diagonally opposed subunits are shown to clarify the position of the central pore axis, and the bound Ca^{2+} ion is shown as a green sphere. In **f**, inset shows expanded view of the boxed region, demonstrating electron density for connectivity in the S6-TRP helix linker that is distinct from other TRP channel structures[14,16,17].

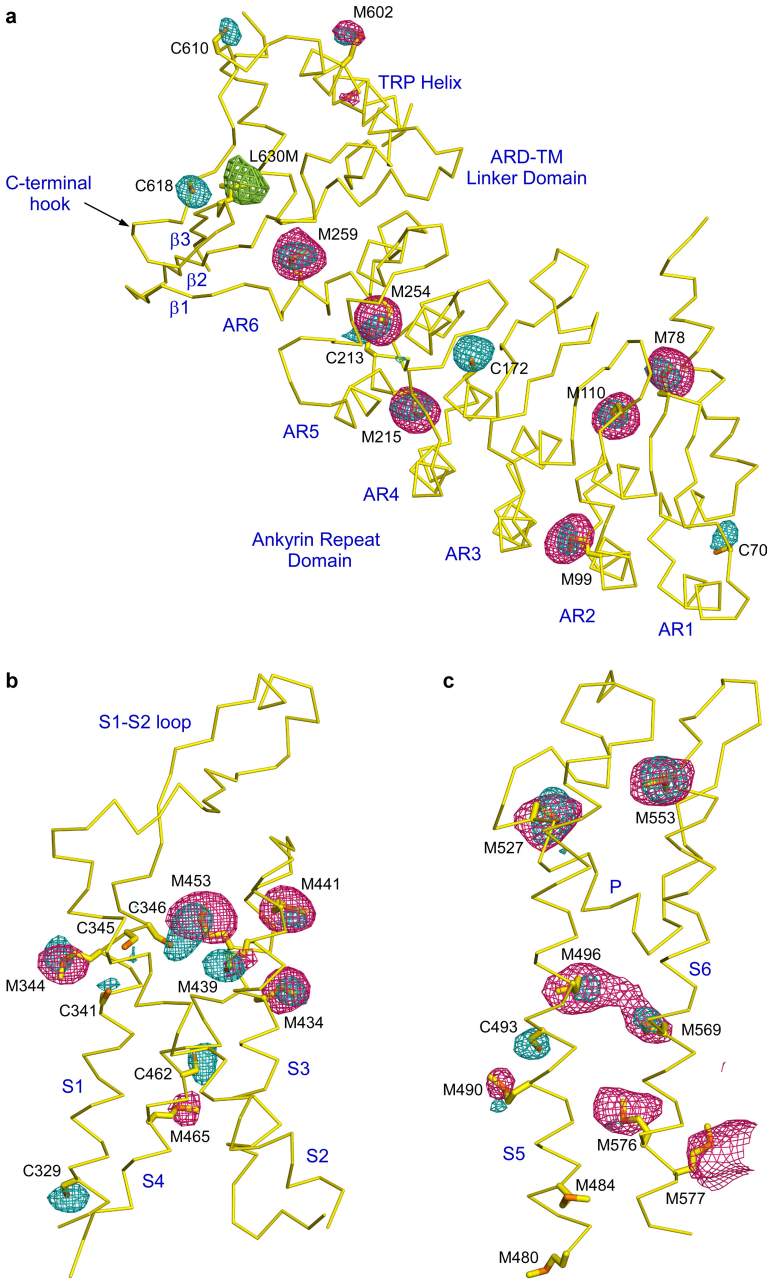

Extended Data Figure 3 | Anomalous difference Fourier maps for sulfur and selenium. a–c, Fragments of the $TRPV6_{cryst}$ model (yellow ribbon) superimposed onto anomalous difference Fourier maps from X-ray diffraction data collected at 1.75 Å from crystals grown in 10 mM Ca^{2+} (cyan mesh, 38–4.59 Å, 3.0σ) and at 0.979 Å from selenomethionine-labelled crystals (pink mesh, 30–5.00 Å, 3.2σ) of $TRPV6_{cryst}$. Anomalous signal collected from a selenomethionine–labelled crystal of $TRPV6_{cryst}$ with L630M substitution (**a**, green mesh, 30–7.20 Å, 3.2σ) was used to aid registry in the C-terminal β3 strand. Domains are labelled in blue. Cysteine and methionine residues are shown as sticks and labelled. Sulfur anomalous difference peaks were observed for all cysteines in the $TRPV6_{cryst}$ model. Selenium anomalous difference peaks were observed for all methionines in the model, except for M480 and M484 in S5, presumably because of flexibility.

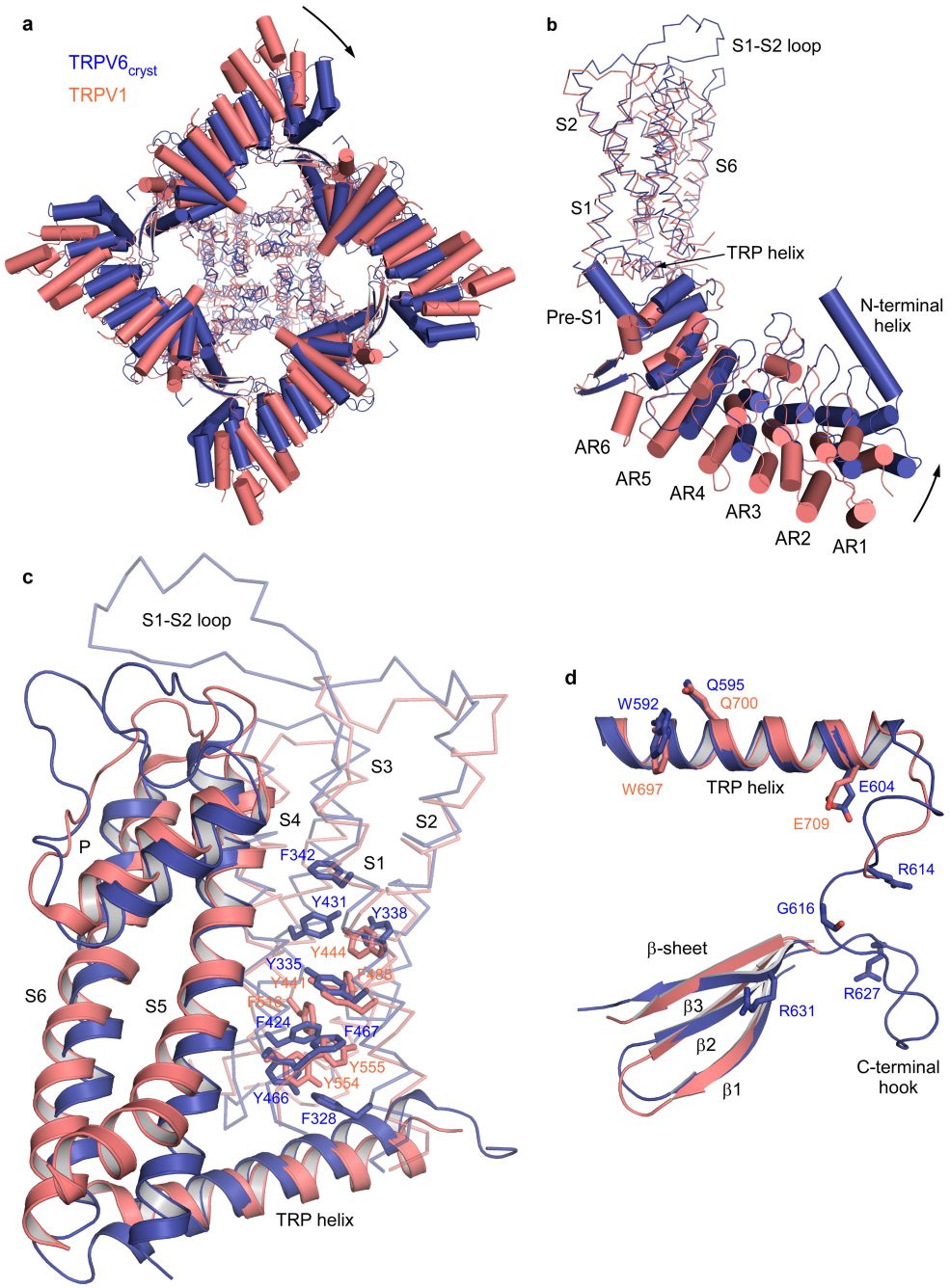

Extended Data Figure 4 | Comparison of TRPV6$_{cryst}$ and TRPV1. **a**, Bottom-up view of TRPV6$_{cryst}$ (blue) and TRPV1 (salmon) tetramers, with ankyrin repeat domain and linker domain helices shown as cylinders. When S1–S4 domains are aligned, as shown, the cytoplasmic skirt of TRPV6 is rotated clockwise with respect to the cytoplasmic skirt of TRPV1. **b**, Side view of TRPV6$_{cryst}$ (blue) and TRPV1 (salmon) monomers with S1–S4 domain based alignment. The ankyrin repeat domain of TRPV1 extends slightly further into the cytoplasm than TRPV6$_{cryst}$. **c**, Alignment of TRPV6$_{cryst}$ (blue) and TRPV1 (salmon) transmembrane domains. Adjacent S1–S4 and pore domains are shown for comparison. Similar to TRPV1, aromatic residues pack against each other to immobilize the TRPV6$_{cryst}$ S1–S4 domain core (shown as sticks). The absence of curvature in S5 and the long extracellular S1–S2 loop protruding towards the pore are distinct features of the TRPV6$_{cryst}$ transmembrane domain. **d**, Alignment of the TRPV6$_{cryst}$ TRP helix, C-terminal hook and three stranded β-sheet with homologous domains in the TRPV1. Conserved residues (Extended Data Fig. 7) are shown in stick representation.

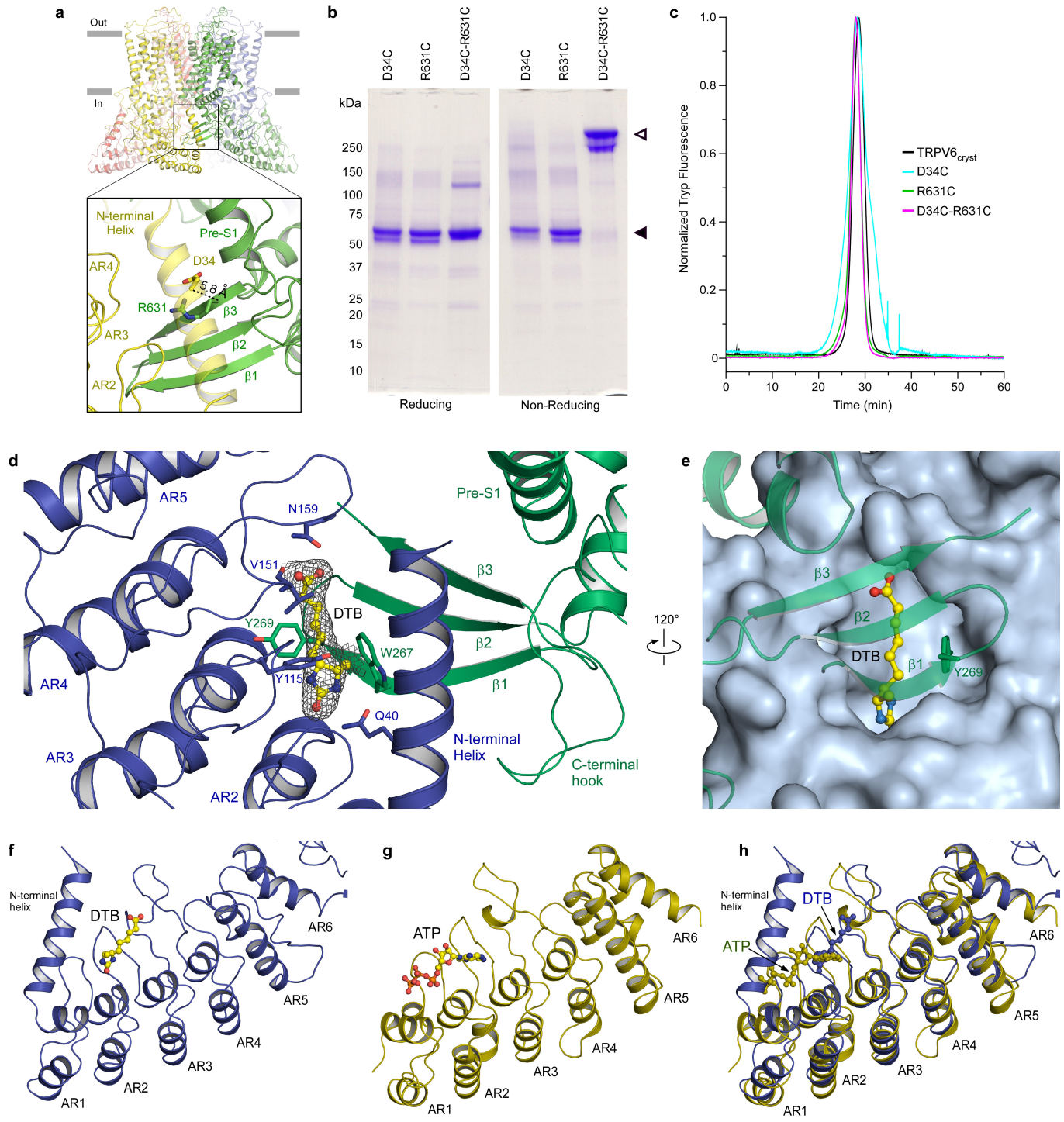

Extended Data Figure 5 | See next page for caption.

Extended Data Figure 5 | Cysteine crosslinking at the intracellular skirt interface and putative desthiobiotin-binding site at the intracellular intersubunit interface. a, The $TRPV6_{cryst}$ tetramer with each subunit coloured differently (top) and expanded view of boxed region (bottom), with cysteine-substituted residues shown as sticks. Dashed line and label show C_α–C_α distance. **b**, SDS–PAGE (4–20% gradient gel) analysis of purified TRPV6 cysteine-substituted mutants in the presence (left) and absence (right) of reducing agent. Cysteines were introduced into a background construct ($TRPV6_{CysKO}$), in which exposed cysteines in $TRPV6_{cryst}$ were mutated to serine or alanine (C14S, C20S, C70A, C610A and C618A) to prevent non-specific aggregation. Positions corresponding to monomer and tetramer bands are indicated by filled and open triangles, respectively. The appearance of a robust band corresponding to covalently crosslinked tetramer in the D34C–R631C double mutant indicates that the interacting N-terminal helix (which precedes the S1–S4 domain) and β3 strand (which follows the TRP helix) are from different protomers. Taken together with the S6-TRP helix linker connectivity (Extended Data Fig. 2f) that is different from TRPV1/2 (refs 14, 16) and TRPA1 (ref. 17), these data suggest a non-swapped arrangement of the pore and S1–S4 domains; if the canonical domain-swapped arrangement were true, the interacting N-terminal helix and β3 strand would be from the same monomer and no crosslinked high molecular mass species would form. However, in the absence of interpretable density for the S4–S5 linker, we suggest cautious interpretation of this domain arrangement. **c**, FSEC analysis of purified $TRPV6_{CysKO}$ crosslink mutants in the absence of reducing agent. Each trace shows a single major peak with elution time corresponding to the $TRPV6_{cryst}$ tetramer (black trace). **d**, **e**, The putative DTB-binding site is composed of a pocket formed by the N-terminal helix and ankyrin repeats 2–4 of one subunit (blue) and the linker domain of an adjacent subunit (green). DTB is shown as ball and stick, with $2F_o - F_c$ density shown as grey mesh (45–3.25 Å, 1.0σ). In **d**, residues that contact DTB are shown as sticks. In **e**, the binding pocket is shown in surface representation. Interestingly, the DTB-binding site overlaps with the ATP-binding site revealed in the ankryin domain crystal structure of TRPV1 (ref. 47), which was later demonstrated to be conserved in TRPV3 and TRPV4 (ref. 48). The presence of DTB close to this location in TRPV6 corroborates the assertion made in ref. 14 that ligands bound in this region modulate activity by perturbing subunit interactions. Further work is necessary to establish a functional role, if any, of DTB-like compounds on TRPV6 function. **f**–**h**, Comparison of the putative DTB-binding site in $TRPV6_{cryst}$ (**f**) and the ATP-binding site in the crystal structure of the TRPV1 ankyrin domain (**g**, PDB accession number 2PNN). DTB and ATP are shown in ball and stick. While the ATP-binding site in TRPV1 is shifted towards ankyrin repeat finger 1, both binding sites are located at intersubunit interfaces, as illustrated when the structures are superimposed (**h**).

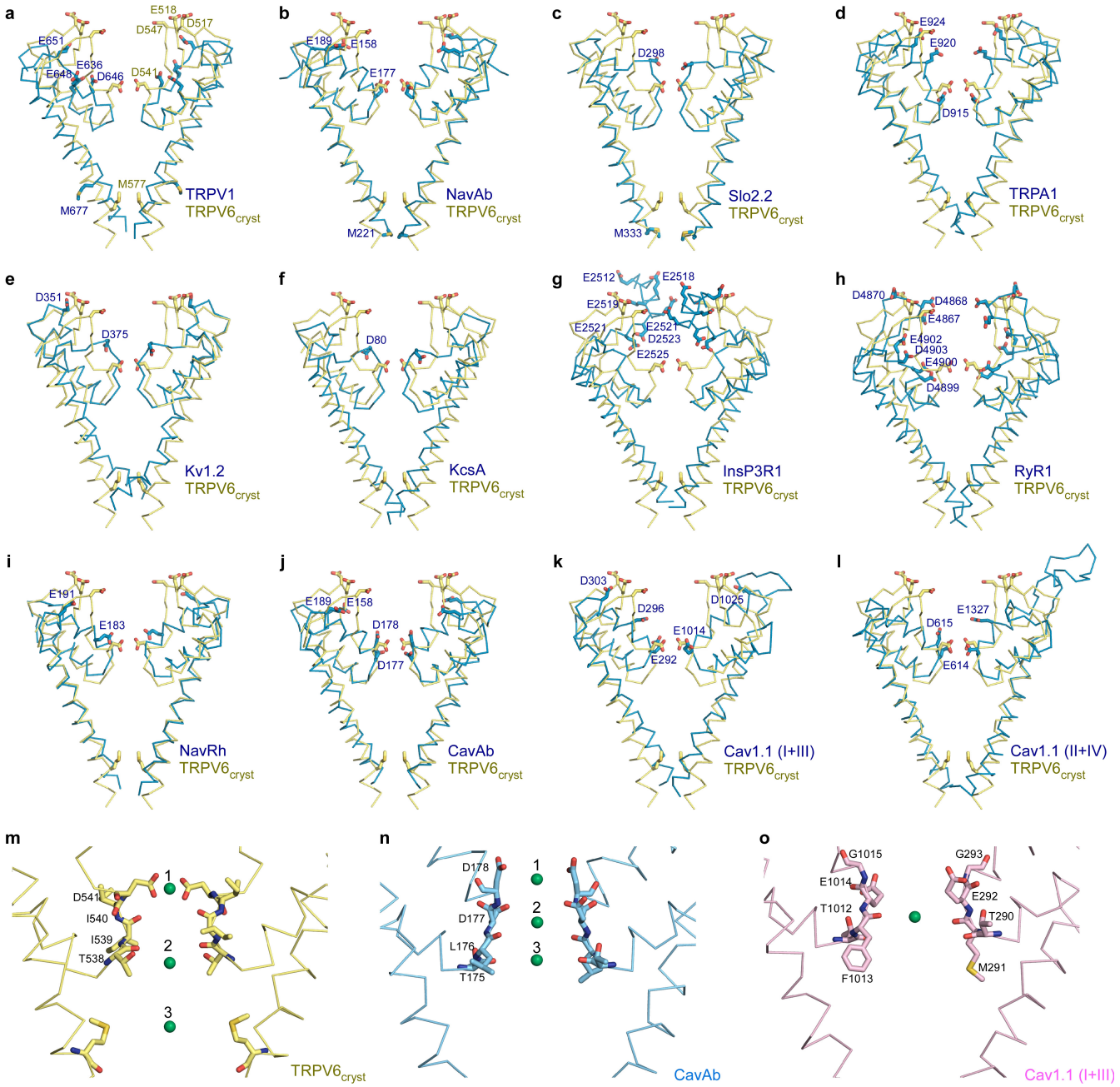

Extended Data Figure 6 | Comparison of the ion channel pore in TRPV6$_{cryst}$ with other tetrameric ion channels. a–l, The pore of TRPV6$_{cryst}$ (yellow ribbon) was aligned with TRPV1 (**a**, PDB accession number 3J5P), Na$_V$Ab (**b**, PDB accession number 3RVY), Slo2.2 (**c**, PDB accession number 5A6E), TRPA1 (**d**, PDB accession number 3J9P), K$_V$1.2 (**e**, PDB accession number 2R9R), KcsA (**f**, PDB accession number 1BL8), InsP$_3$R1 (**g**, PDB accession number 3JAV), RyR1 (**h**, PDB accession number 3J8H), Na$_V$Rh (**i**, PDB accession number 4DXW), Ca$_V$Ab (**j**, PDB accession number 4MVM), Ca$_V$1.1 domains I and III (**k**, PDB accession number 3JBR) and Ca$_V$1.1 domains II and IV (**l**, PDB accession number 3JBR). In each of the alignments, acidic residues located at or close to the selectivity filter region are shown as sticks for comparison. Notably, structures of Ca^{2+}-permeable channels (**a**, **d**, **g**, **h**, **j–l**) display a high concentration of acidic residues in the outer pore region. In **a–c**, methionine residues close to the S6 bundle crossing are shown as sticks. Notably, the methionine at the lower gate points away from the pore in TRPV1 (**a**), despite high sequence conservation in this region among TRPV channels (Extended Data Fig. 7). In Slo2.2 (**b**) and Na$_V$Ab (**c**), methionine side chains occlude the lower gate as in TRPV6$_{cryst}$, indicating that the closed conformation of the lower gate can be chemically similar for Na^+-, K^+- and Ca^{2+}-selective channels. **m–o**, Comparison of calcium-binding sites in TRPV6$_{cryst}$ (**m**), the engineered voltage gated Ca^{2+} channel Ca$_V$Ab (**n**) and the putative Ca^{2+} site in Cav1.1 (**o**, domains I and III are shown). Residues constituting the selectivity filters are shown in stick representation. Ca^{2+} ions are shown as green spheres. Sites 1 and 2 from TRPV6$_{cryst}$ overlap with the positions of sites 1 and 3 from Ca$_V$Ab, respectively. While it has been proposed that, owing to electrostatic repulsion, sites 1, 2 and 3 cannot be simultaneously occupied in Ca$_V$Ab, distances between Ca^{2+}-binding sites in TRPV6$_{cryst}$ are sufficiently large such that they can be simultaneously occupied. The putative Ca^{2+} site in Ca$_V$1.1 is near the equivalent location of site 2 in Ca$_V$Ab.

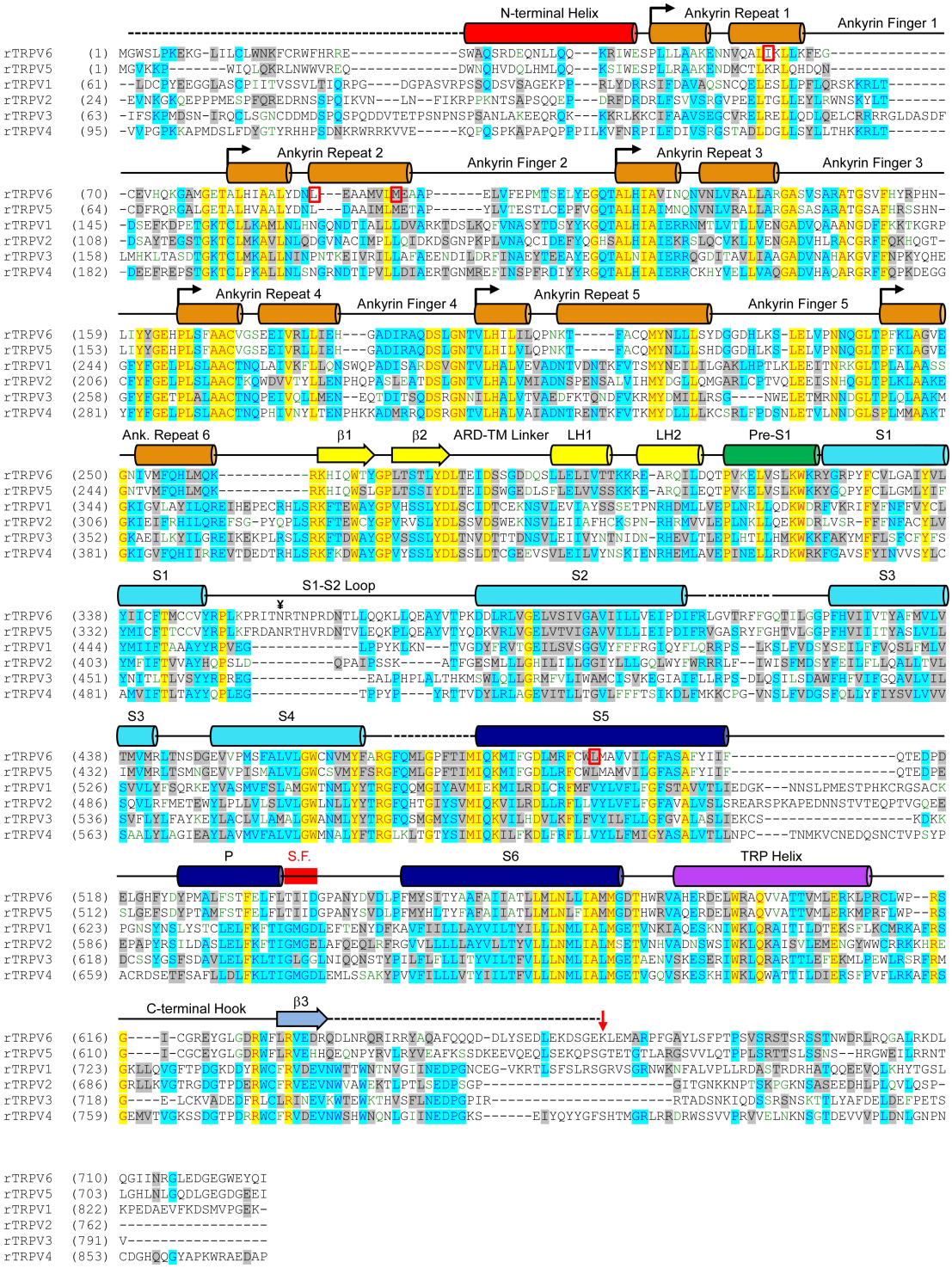

Extended Data Figure 7 | Sequence alignment of rat TRPV subtypes. Secondary structure elements are depicted above the sequence as cylinders (α-helices), arrows (β-strands) and lines (loops). Dashed lines show residues in the TRPV6$_{cryst}$ construct not included in the TRPV6$_{cryst}$ structural model. Red boxes and a red arrow highlight substitution mutations and the C-terminal truncation point in TRPV6$_{cryst}$, respectively (see Methods). The ¥ symbol marks the N-linked glycosylation site in the extracellular loop connecting S1 and S2 conserved in TRPV6 (and TRPV5) channels. The thick red line marks the location of the selectivity filter.

a

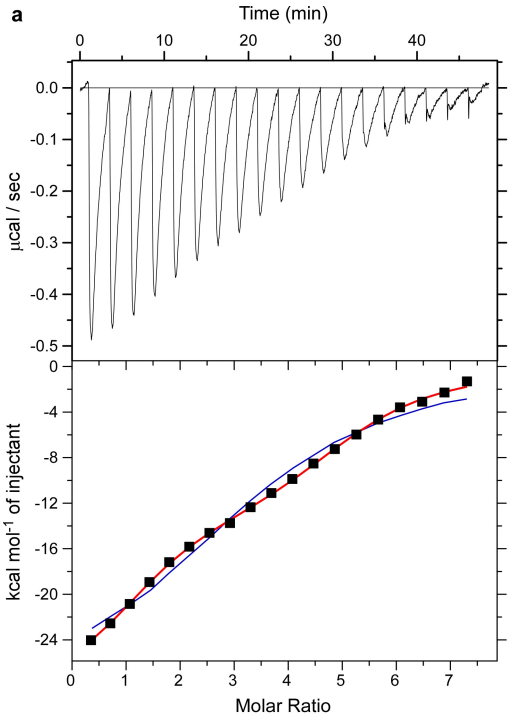

b

Parameter	Value
n_1	1.23 ± 0.08 sites
K_1	1.54 ± 0.04 µM^{-1}
ΔH_1	-29.3 ± 2.2 kcal/mol
ΔS_1	-70 cal/mol/deg
ΔG_1	-8.44 ± 0.16 kcal/mol
n_2	3.74 ± 0.09 sites
K_2	0.182 ± 0.022 µM^{-1}
ΔH_2	-13.8 ± 1.3 kcal/mol
ΔS_2	-22.2 cal/mol/deg
ΔG_2	-7.18 ± 0.07 kcal/mol

c

	Ca^{2+}	Ba^{2+}	Gd^{3+}
Sites			
Site 1	10.2	4.4	31.40
Site 2	7.5	14.6	–
Site 3	3.6	4.6	–
Recruitment Site	–	4.2	8.0

Extended Data Figure 8 | Isothermal titration calorimetry analysis of TRPV6 interaction with Gd^{3+} and anomalous peak amplitudes. a, Gd^{3+} in the syringe (700 µM) was titrated into TRPV6 (6.38 µM) loaded into the cell. Measurements were performed at 25 °C. Top, the raw data for nineteen 2-µl injections of Gd^{3+}. The area of each injection peak is equal to the total heat released from that injection. Bottom, the integrated heat per injection versus molar ratio. Binding of Gd^{3+} to TRPV6 was analysed using models with one and two types of binding site. A model with one type of binding site was not sufficient to explain the binding isotherm (blue line). In contrast, analyses of the binding isotherm using the model with two types of binding site, according to equation $Q_i^{tot} = V_0 M_{tot}((n_1 \Delta H_1 K_1[X]/(1 + K_1[X])) + (n_2 \Delta H_2 K_2[X]/(1 + K_2[X])))$, where Q_i^{tot} is total heat after the ith injection, V_0 is the volume of calorimetric cell, M_{tot} is the bulk concentration of protein, $[X]$ is the free concentration of Gd^{3+}, n_1 and n_2 are the numbers of type 1 and 2 sites, K_1 and K_2 are the observed equilibrium constants for each type of the sites and ΔH_1 and ΔH_2 are the corresponding enthalpy changes, satisfactorily described the data (red line), and the corresponding values of thermodynamic parameters are given in **b**. The values of ΔG and $T\Delta S$ were calculated using the following relationships: $\Delta G = -RT \ln K$ and $\Delta G = \Delta H - T\Delta S$. **b**, Table showing the parameters of experimental data fitting to the model with two types of Gd^{3+}-binding site. The straightforward interpretation of the ITC results is that the ITC type 1 ($n \approx 1$) and type 2 ($n \approx 4$) sites represent the main (site 1) and recruitment sites identified crystallographically (Fig. 4e, f). Correspondingly, the affinity to Gd^{3+} for recruitment sites is ~10 times lower than for site 1. **c**, Table showing anomalous peak amplitudes in σ calculated from data collected for Ca^{2+} (38–4.59 Å), Ba^{2+} (38–4.59 Å) and Gd^{3+} (38–4.59 Å). No numbers are given if the peaks were not observed.

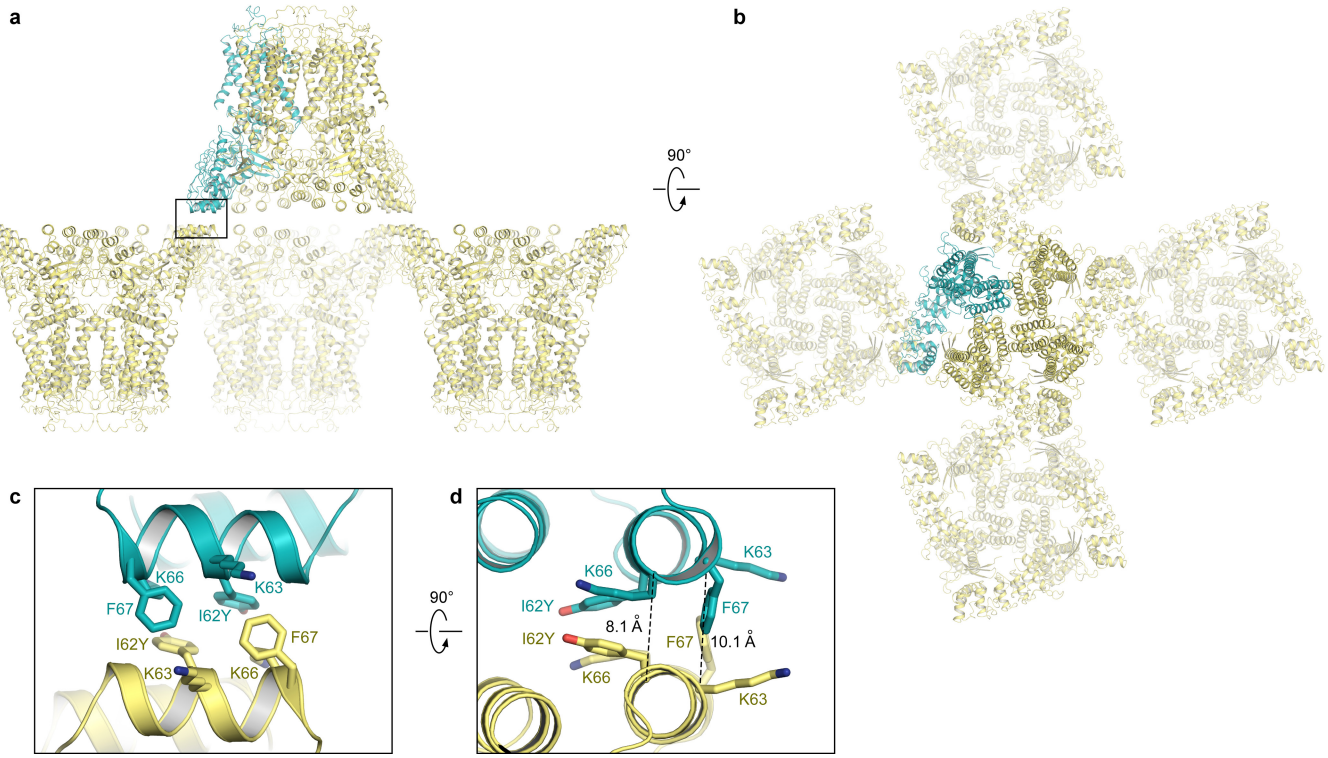

Extended Data Figure 9 | Crystal lattice contact of TRPV6$_{cryst}$. **a**, **b**, Two views of TRPV6$_{cryst}$ crystal packing in the $P42_12$ space group. A single TRPV6$_{cryst}$ protomer in the asymmetric unit is shown in blue. **c**, **d**, Close-up views of boxed region in **a**. Contacting residues are shown in stick, and C_α–C_α distances are labelled in **d**. The crystal contact is apparently mediated by cation-π and/or hydrogen bonding interactions between these residues. Crystals in the $P42_12$ space group did not form when the native isoleucine was present at position 62.

Extended Data Table 1 | Data collection and refinement statistics

	Native	Ba^{2+}	Ca^{2+}	Gd^{3+}	L630M-SeMet	SeMet
Data Collection						
Beamline	APS-24ID-C	APS-24ID-C	APS-24ID-C	APS-24ID-C	APS-24ID-E	APS-24ID-E
Space group	$P42_12$	$P42_12$	$P42_12$	$P42_12$	$P42_12$	$P42_12$
Cell dimensions a, b, c, (Å)	143.81 143.81 113.22	144.35 144.35 113.37	144.35 144.35 113.37	144.35 144.35 113.37	143.60 143.60 114.44	143.95 143.95 113.04
α, β, γ (^{0})	90 90 90	90 90 90	90 90 90	90 90 90	90 90 90	90 90 90
Wavelength (Å)	0.9791	1.75	1.75	1.7101	0.9792	0.9792
Resolution (Å)*	44.48 - 3.25 (3.36 - 3.25)	49.56 - 3.85 (3.99 - 3.85)	49.56 - 3.65 (3.78 - 3.65)	50.00 - 3.80 (3.936 - 3.80)	40.00 - 7.20 (7.46 - 7.20)	40.00 - 5.00 (5.18 - 5.00)
Completeness (%)*	96.0 (94.7)	99.5 (95.4)	99.9 (99.8)	99.5 (97.3)	99.9 (100.0)	100.0 (100.0)
Redundancy*	8.7 (9.2)	15.4 (13.9)	26.5 (17.2)	11.4 (6.4)	16.3 (17.5)	13.7 (13.9)
$\|I/\sigma\|$*	16.9 (1.3)	15.2 (1.5)	25.0 (2.4)	19.4 (1.6)	27.3 (6.3)	21.8 (4.7)
R_{meas} (%)*	9.8 (132.6)	13.1 (228.5)	10.6 (143.1)	8.9 (120.7)	20.7 (86.4)	19.2 (93.5)
$CC_{1/2}$	99.8 (85.7)	98.0 (76.8)	99.5 (85.7)	99.9 (63.7)	98.5 (89.8)	98.3 (92.5)
Refinement						
Resolution (Å)*	44.48 - 3.25 (3.36 - 3.25)	49.56 - 3.85 (3.99 - 3.85)	50.00 - 3.65 (3.78 -3.65)	49.56 - 3.80 (3.94 - 3.80)		
Completeness (%)	96 (93.8)	100 (99.9)	100 (99.9)	99 (96.9)		
Number of reflections	18531 (1724)	21705 (2187)	25439 (2521)	22443 (2170)		
R_{work}/R_{free}	0.273/0.289	0.291/0.326	0.276/0.281	0.298/0.321		
Number of atoms						
Total	4747	4775	4735	4759		
Ligand	16	19	18	17		
B-factor (Å^2)						
Protein	120.5	143.8	135.1	144.23		
Ligand	77.27	136.75	24.14	178.86		
RMS deviations						
Bond length (Å)	0.003	0.002	0.003	0.002		
Bond angles (^{0})	0.7	0.62	0.62	0.63		
Ramachandran						
Favored (%)	93.6	92.9	93.7	92.8		
Allowed (%)	5.7	6.93	6.13	7.03		
Disallowed (%)	0.17	0.17	0.17	0.17		

*Highest resolution shell in parentheses.
Five per cent of reflections were used for the calculation of R_{free}.